Metastable neural dynamics in Alzheimer's disease are disrupted by lesions to the structural connectome.

Thomas Alderson[1]*, Arun L.W. Bokde[3], J.A.Scott. Kelso[1,2], Liam Maguire[1], Damien Coyle[1], Alzheimer's Disease Neuroimaging Initiative**

[1]Intelligent Systems Research Centre, Ulster University, UK

[2]Center for Complex Systems and Brain Sciences, Florida Atlantic University, Boca Raton, USA

[3]Trintity College Institute of Neuroscience and Cognitive Systems Group, Discipline of Psychiatry, School of Medicine, Trinity College Dublin, Ireland

**Data used in preparation of this article were obtained from the Alzheimer's Disease Neuroimaging Initiative (ADNI) database (adni.loni.usc.edu). As such, the investigators within the ADNI contributed to the design and implementation of ADNI and/or provided data but did not participate in analysis or writing of this report. A complete listing of ADNI investigators can be found at: http://adni.loni.usc.edu/wp-content/uploads/how_to_apply/ADNI_Acknowledgement_List.pdf

Address correspondence to Thomas Alderson, Intelligent Systems Research Centre, School of Computing, Engineering & Intelligent Systems, Magee Campus, Londonderry, BT48 7JL. Email: thomashenryalderson@gmail.com

Abstract

Current theory suggests brain regions interact to reconcile the competing demands of integration and segregation by leveraging metastable dynamics. An emerging consensus recognises the importance of metastability in healthy neural dynamics where the transition between network states over time is dependent upon the structural connectivity between brain regions. In Alzheimer's disease (AD) – the most common form of dementia – these couplings are progressively weakened, metastability of neural dynamics are reduced and cognitive ability is impaired. Accordingly, we use a joint empirical and computational

approach to reveal how behaviourally relevant changes in neural metastability are contingent on the structural integrity of the anatomical connectome. We estimate the metastability of fMRI BOLD signal in subjects from across the AD spectrum and in healthy controls and demonstrate the dissociable effects of structural disconnection on synchrony versus metastability. In addition, we reveal the critical role of metastability in general cognition by demonstrating the link between an individuals cognitive performance and their metastable neural dynamic. Finally, using whole-brain computer modelling, we demonstrate how a healthy neural dynamic is conditioned upon the topological integrity of the structural connectome. Overall, the results of our joint computational and empirical analysis suggest an important causal relationship between metastable neural dynamics, cognition, and the structural efficiency of the anatomical connectome.

Keywords

Alzheimer's disease, metastability, structural connectome, whole-brain modelling, Kuramoto, DTI

Introduction

Duality lies at the origin of many branches of science and philosophy wherein seemingly opposite forces interact to form a dynamic system in which the whole is greater than the sum of its assembled parts (Kelso, 2008). Rather than viewing apparently contrary phenomena as irreconcilable features of the world, the "philosophy of complementary pairs" recognises their mutually related nature while simultaneously honouring their differences (Engstrøm and Scott Kelso, 2008). One such "complementary pair" may be found in the dialogue between synchrony and asynchrony in the brain – a reflection of the growing consensus that the complementary nature of integrating and segregating tendencies is an essential feature of how brains operate (Bressler and Kelso, 2001, 2016). Accordingly, several developmental, traumatic, and neurodegenerative conditions could be described as an imbalance in the optimal working point of synchrony and asynchrony (Uhlhaas and Singer, 2006; Uhlhaas, 2015). Epilepsy, for example, could be described in terms of excess neural order – synchrony has become a tyrant. Conversely, several neuropsychiatric conditions, in which the structure of the brain is abnormal e.g.

schizophrenia, autism, and Alzheimer's disease (AD) are defined by an excess of neural disorder or asynchrony.

Recently, these observations have been placed on firm empirical and theoretical ground by appealing to a dynamical regime known as metastability (Kelso, 1995, 2012, Tognoli and Kelso, 2009, 2014a, 2014b), in which the tendency for local regions to express their local independence is balanced with the requirement to integrate and coordinate information globally (Deco et al., 2015). The advent of diffusion tensor imaging (DTI) has permitted these observations to be tested in-silico (Deco and Kringelbach, 2014). Here, networks of oscillators interact on a backbone of inferred inter-regional white matter known as the structural connectome (Ghosh et al., 2008; Deco et al., 2009, 2013a, 2013b; Honey et al., 2010; Deco and Jirsa, 2012; Cabral et al., 2014; Breakspear, 2017). In this way, connectomic-based computer modelling permits an analysis of the structural connectivity's role in shaping the brain's functional architecture. The relationship between the connectome's structural integrity and metastable neural dynamics has previously been investigated in a model of traumatic brain injury (Hellyer et al., 2015). In this work, Hellyer et al., (2015) observed that decreases in neural metastability were behaviourally relevant and linked to damage within the connectome. In other work, Váša et al., (2015) appraised the impact of removing individual nodes on metastability in a systematic manner.

The relationship between structure and function is also altered in Alzheimer's disease – the most common form of dementia. AD presents as a steadily worsening constellation of symptoms that mirror the gradual accumulation of misfolded amyloid protein and neurofibrillary tangles. Accordingly, patients are situated on a continuum of phenotypes related to cognitive status ranging from mild memory loss in mild cognitive impairment (MCI) through to advanced cognitive and behavioural deficits in overt AD. The transition between diagnostic categories is marked by a reliable asymptotic decline in overall neural metastability that conforms to the pathophysiological staging of the disease (Córdova-Palomera et al., 2017; Demirtaş et al., 2017).

In light of the foregoing, the present paper utilises a dual empirical and computational approach to investigate the relationship between topological properties of the structural connectome, metastable neural dynamics, and cognitive performance in healthy control (HC) subjects and in patients from across the AD spectrum. For this reason, resting state functional and structural neuroimaging data were obtained from the Alzheimer's Disease Neuroimaging Initiative (ADNI; Mueller et al., 2005) in three subject groups including

healthy control (HC), mild cognitive impairment, and AD. The inclusion of resting state or task-free fMRI into the functional imaging suite has been especially advantageous to dementia researchers where subject compliance can be an issue – here subjects are simply required to lie down and stay awake. In the absence of an assigned task, the ultra-low frequency (< 0.1HZ) blood oxygen level dependent (BOLD) signal demonstrates several distinct patterns of covariance across the cortex known as resting state networks (Damoiseaux et al., 2006). Several neurodegenerative disorders including AD (Buckner et al., 2008) show dissociable patterns of abnormal structure and function in these networks consistent with a disconnection syndrome (Seeley et al., 2009). Converging lines of evidence from experimental neuropathology (Braak and Braak, 1991), neuroimaging (Greicius et al., 2004; Buckner et al., 2005), and transgenic animal studies (Palop and Mucke, 2010) support the contention that AD, in part, represents a disconnection syndrome. Indeed, recent empirical findings emphasise the importance of early inter-areal white matter connectivity in AD pathogenesis (O'Dwyer et al., 2011a, 2011b) and challenge the conventional view that AD solely represents a disease of the grey matter (Sachdev et al., 2013). Contemporary observations suggests that 1), white matter abnormalities occur while grey matter is still relatively preserved (Brun and Englund, 1986; de la Monte, 1989; Heise et al., 2010; Zhuang et al., 2012); 2), that demyelination and axonal abnormalities occur before the formation of amyloid plaque and neurofibrillary tangles (Desai et al., 2009, 2010); and 3), that impaired axonal transport not only precedes the downstream production of grey matter amyloid but actively participates in its formation (Wirths et al., 2006, 2007; Smith et al., 2007).

The paper is structured as follows. We first estimate the global neural metastability of fMRI BOLD signal in resting state networks across the three subject populations (HC/MCI/AD). Next, we evaluate the impact of macroscopic structural disconnection on large-scale neural metastability. For this we employ whole-brain computer models informed by subject-level anatomical connectivity. We then explore the relationship between local network topology in the healthy connectome and damage at the regional level between nodes of the computer model. Next, we investigate how damage to the large-scale structural topology of the connectome effects the metastability of simulated neural dynamics. We subsequently identify differences in synchrony and metastability of fMRI BOLD signal in patients and controls using the network based statistic (NBS). Finally, we

ascertain if the empirical estimates of brain-wide neural metastability are linked to cognitive ability.

We found that 1), macroscopic damage to the structural connectome elicited comparable reductions in simulated metastability to that observed in the empirical data; 2), damage to the computer model's connectivity was centred around highly connected nodes; 3), reductions in simulated neural metastability were the product of abnormal network topology; 4), widespread decreases in metastability between empirical resting state networks in AD subjects contrasted sharply with more focal decreases in synchrony; and 5), reductions in large-scale metastability of fMRI BOLD signal correlated with cognitive test scores across the AD spectrum. Overall, the results of our joint computational modelling and empirical analysis suggest a key linkage between metastable neural dynamics, cognition and the structural integrity of the human brain.

Materials and Methods

2.1 Data overview

Data were obtained from the ADNI database (http://adni.loni.usc.edu). In the present study, we analysed baseline visit data collected from HC, MCI, and AD subjects who were recruited for ADNI-2. All subjects and their study partners completed the informed consent process, and the study protocols were reviewed and approved by the Institutional Review Board at each ADNI data collection site.

The ADNI was launched in 2003 by the National Institute on Aging, the National Institute of Biomedical Imaging and Bioengineering, the Food and Drug Administration, private pharmaceutical companies and non-profit organizations as a public-private partnership. The primary goal of ADNI has been to test whether neuroimaging, fluid and genetic biomarkers, and cognitive assessments can be combined to measure the progression of MCI and early AD. Additional information is available at www.adni-info.org.

2.2 Subjects

All ADNI participants underwent a "screening" visit, during which they completed the Mini-Mental State Examination (MMSE; Folstein et al., 1975), Clinical Dementia Rating (CDR; Hughes et al., 1982) scale, and the Wechsler Memory Scale-Revised (WMS-R; Wechsler, 1987) Logical Memory II test. Three cohorts composed of 36 HC, 33 MCI, and 34 AD were

included in the functional magnetic resonance imaging (fMRI; Table S1) study and 30 in each group were included in the diffusion tensor imaging (DTI; Table S2) study. Since ADNI currently does not collect multi-modal DTI/fMRI imaging data for the same subjects, the DTI and fMRI cohorts comprised different individuals. For this reason we are unable to directly compare structural and functional data at the subject-level and instead compare participants at the group-level. We justify this by appealing to the stereotypical spatio-temporal staging of neuropathology (Braak and Braak, 1991; Braak et al., 1999) and biomarkers (Jack et al., 2013) across individuals. The detailed criteria used to define the three groups (HC/MCI/AD) are provided as supplementary information along with full participant demographics.

2.3 MRI data acquisition

Standard protocols were used to acquire functional, structural, and diffusion tensor image data. Whole-brain structural and functional data were acquired on a 3.0 Tesla Philips Intera MR system (Philips, Best, Netherlands) equipped with an eight channel head coil and sensitivity encoding (SENSE) with a reduction factor of one. A high-resolution anatomical T1-weighted sagittal 3D MP-RAGE image was acquired with the following parameters: 1 x 1 mm^2 in-plane resolution, 1.2 mm slice thickness, TR = 6.8 ms, TE = 3.2 ms, flip angle = 9º, 256 x 240 mm FOV, and 256 x 240 matrix. Resting-state fMRI data were also acquired. Subjects were instructed to keep their eyes open during the scan and fixate on a cross hair in the centre of a screen located behind the MR scanner, visible via a mirror. Each volume of data covered the entire brain with 48 slices, and the slices were acquired in interleaved sequence from inferior to superior direction. One hundred and forty volumes were acquired. The BOLD signal changes were measured using a T2*-weighted echo-planar imaging sequence with the following parameters: 3.3 x 3.3 mm^2 in-plane resolution, 3.3 mm slice thickness, TR = 3000 ms, TE = 30 ms, flip angle = 80º, 212 x 198.75 mm^2 FOV, and 64 x 59 matrix.

Likewise, whole-brain structural and diffusion tensor data were acquired on a 3.0 Tesla General Electric Signa HDxt MR system (General Electric Medical Systems, Milwaukee, WI, USA) equipped with an 8HRBRAIN head coil. A high-resolution anatomical T1-weighted sagittal 3D IR-SPGR image was acquired with the following parameters: 1 x 1 mm2 in-plane resolution, 1.2 mm slice thickness, TR = 7 ms, TE = 2.85 ms, flip angle = 11º, 256 x 240 mm FOV, and 256 x 240 matrix. Single-shot spin echo-planar imaging was used to acquire the diffusion weighted image data with following parameters: 2.7 x 2.7

mm^2 in-plane resolution and 2.7 mm slice thickness, TR = 13000 ms, TE = 68.4 ms, flip angle = 90º, 350 mm FOV, and 129 x 129 matrix. Diffusion gradients were applied in 41 isotropically distributed orientations with b = 1000 s/mm^2, and five images with b = 0 s/mm^2.

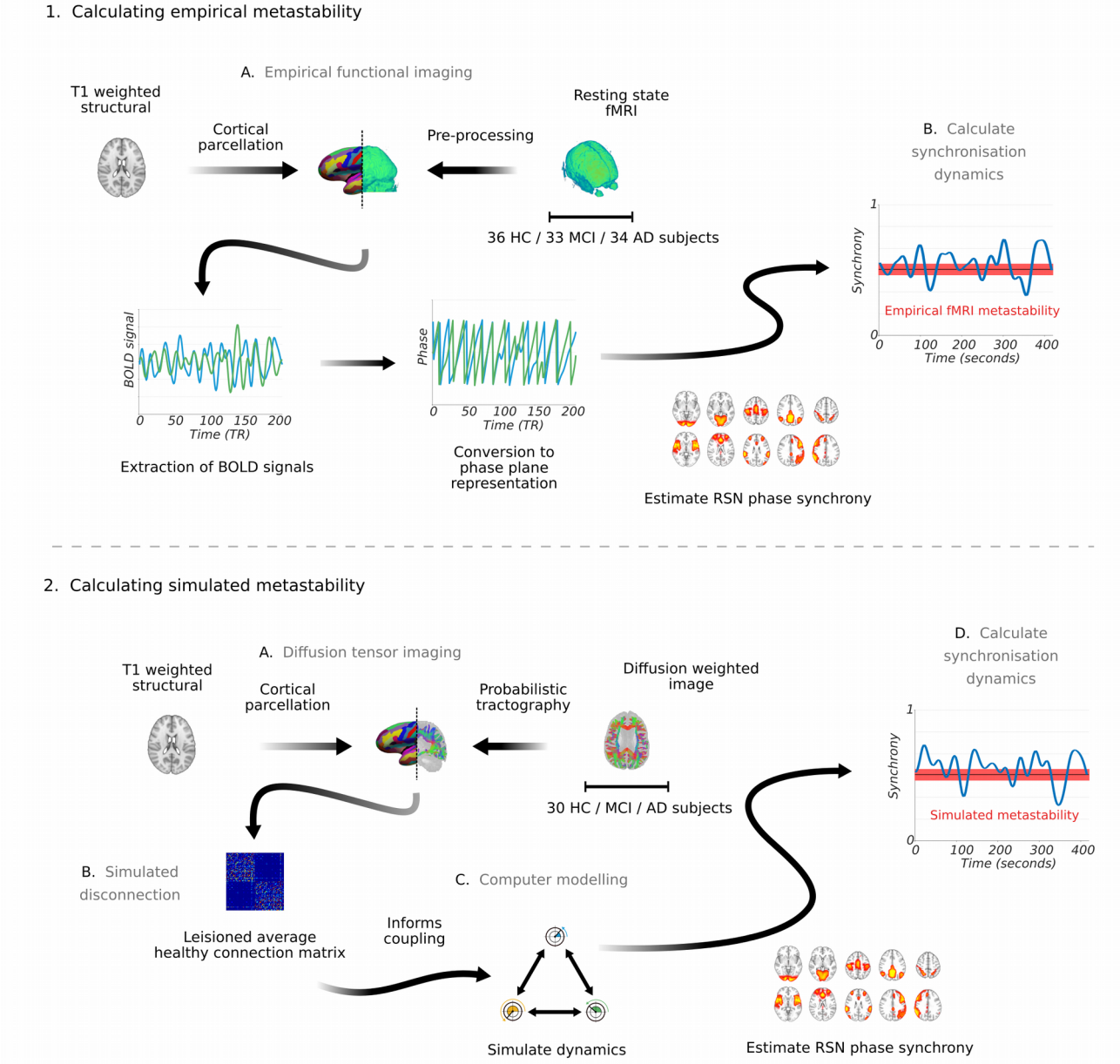

Figure 1: Overview of experimental design. Resting state fMRI BOLD signal was used to calculate empirical metastability across three groups including HC, MCI, and AD (top). 1.A, Each subject's T1-weighted structural image was parcellated into 148 regions from which average BOLD signal was extracted. Time series were then converted into complex phase plane representation using the Hilbert transform. 1.B, Estimates of resting state network metastability were then calculated. DTI data across the same three groups were used to inform the coupling strength between nodes in a simple oscillator model (bottom). 2.A, A subject's T1-weighted image was parcellated into 148 distinct regions which were subsequently used to constrain tractography. 2.B, Individual connectivity matrices were created for each clinical subject by lesioning the average control connectivity in tracts that significantly deviated from healthy control values. 2.C, Subject-level whole-brain computer models were constructed with coupling informed by the anatomical data. 2.D, Simulated phase output was subsequently used to estimate resting state network metastability.

2.4 Overview of MRI data analysis

The processing steps approximated the procedures outlined in the automated personalised processing pipeline (Schirner et al., 2015) and comprised 1) pre-processing of anatomical T1-weighted images, cortical reconstruction, tessellation and parcellation into 148 3D volume masks; 2) transformation of anatomical masks to fMRI space; 3) processing of fMRI data and extraction of mean BOLD signal from each 3D volume mask for calculating pairwise phase relations; 4) transformation of anatomical masks to diffusion space; 5) processing of diffusion weighted data and tractography between pairwise 3D volume masks to derive structural connectivity and mean fractional anisotropy (FA) matrices. FA corresponds to the primary direction of water molecule diffusion within a tract. An overview of the steps are provided in Figure 1.

The above workflow was employed to 1) estimate the average structural connectivity of controls based on DTI track fibre density i.e. the healthy template; and 2) estimate individual FA matrices for each MCI and AD subject. Subject-level connectomes were derived by lesioning the healthy template using each clinical subject's FA matrix (see: Generating subject-level structural connectivity). The resulting matrices then informed coupling strength between nodes in a simple oscillator model (see: Constructing the cortical network model).

2.5 Anatomical MRI data analysis

The Freesurfer image analysis suite (http://surfer.nmr.mgh.harvard.edu) performed cortical reconstruction and volumetric segmentation based on the high resolution T1 weighted images. Briefly, these steps included motion correction (Reuter et al., 2010); intensity normalisation (Sled et al., 1998), skull stripping; removal of non-brain tissue, brain mask generation, cortical reconstruction, white matter and sub-cortical segmentation (Fischl et al., 2002, 2004a), cortical tessellation (Fischl et al., 2001; Ségonne et al., 2007) generating grey-white matter interface surface-triangulations, and probabilistic atlas based cortical parcellation (Fischl et al., 2004b; Desikan et al., 2006) using the 2009 Destrieux atlas producing a cortical parcellation with 148 independent sulcal and gyral regions.

2.6 Empirical DTI data analysis and tractography

Pre-processing of the diffusion MRI data included eddy current and motion correction with re-orientation of b-vectors. The b-zero image was linearly registered to the subject's

anatomical T1-weighted image; the resulting transformation rule was stored for later use (see: Empirical fMRI data analysis).

Tractography was constrained by seed, target and stop masks. Masks were transformed from individual anatomical to individual diffusion space. The grey-white matter interface surface triangulation was dilated into a 3D volume, labelled to match the adjacent cortical parcellation and split into 148 separate masks for use as seed and target regions. Tracks exiting the union of grey-white matter interface and cortical white matter were regarded as spurious and terminated. Registrations were performed using the FSL (FMRIB's Software Library, www.fmrib.ox.ac.uk/fsl) software package tool FLIRT (Jenkinson and Smith, 2001; Jenkinson et al., 2002; Greve and Fischl, 2009) and FNIRTs (Andersson et al., 2007).

Probabilistic white matter tractography was performed on the diffusion weighted images using the MRtrix3 software package (http://www.mrtrix.org). Crossing fibres were resolved using the constrained spherical deconvolution algorithm (Tournier et al., 2004, 2012). MRtrix3 pre-processing included computing the diffusion tensor images (or diffusion ellipsoids) for each voxel from which fractional anisotropy (FA) images were subsequently generated. To exclude noise, these were masked by the binary white matter parcellation created previously. Tracks were initiated from randomly distributed seed points within each voxel of the seed mask. Tracks successfully propagating from seed i to target mask j defined a connectivity matrix $C(i,j)$ of size $C_{148\times148}$.

To mitigate bias associated with using seed and target masks of different sizes, tractography was performed in both directions; from seed to target mask $C(i,j)$ and from target to seed mask $C(j,i)$ with each set of tracks being consolidated into a single entry. The seed mask voxel and corresponding target mask voxel were identified and recorded for each track. To address the uncertainty surrounding the relationship between the number of tracks generated for a given pathway and the synaptic strength of that pathway, only distinct connections between seed and target voxels contributed toward overall track count. Track counts were subsequently converted into track density by dividing total track count between region i and region j by total seed and target mask volume and normalising between zero and one. Finally, the mean FA of each fibre bundle was recorded in matrix $FA(i,j)$ of size $FA_{148\times148}$.

2.7 Empirical fMRI data analysis

Excessive peaks in the resting state fMRI time series were first removed using AFNI's (https://afni.nimh.nih.gov/afni) 3dDespike script. Functional connectivity matrices for each subject were then extracted using the FSL software package. Registration to high resolution structural and standard space images was performed using FLIRT and FNIRT respectively. FMRI data processing was carried out using FEAT (FMRI Expert Analysis Tool) Version 6.00. The following pre-statistics processing was applied: motion correction using MCFLIRT, slice-timing correction using Fourier-space time-series phase-shifting, non-brain removal using BET, spatial smoothing using a Gaussian kernel of FWHM 3.0mm, and grand-mean intensity normalisation of the entire 4D dataset by a single multiplicative factor. The first five image volumes were deleted to exclude possible T1-related saturation effects.

The Freesurfer cortical parcellation was transformed to functional space by inverting the functional to T1 structural image transformation rule acquired earlier as part of the diffusion MRI preprocessing pipeline. To account for non-neural sources of physiological noise and head movement, the signals from white matter, cerebrospinal fluid and the six motion parameter time courses estimated by MCFLIRT were regressed out of the functional time series. The empirical BOLD signals were bandpassed filtered in the functionally relevant 0.04 – 0.07 Hz narrowband range to avoid including artefactual correlations and obtain meaningful signal phases (Glerean et al., 2012). Finally, the mean BOLD signal was extracted from each region in the T1-derived cortical parcellation. An overview of the steps are provided in Figure 1.

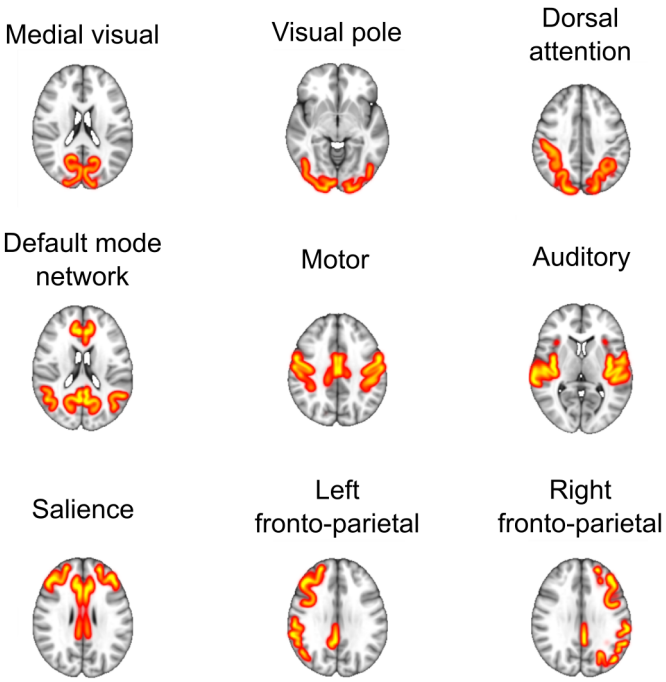

Figure 2: Nine canonical resting state networks reconstructed in MNI 152 space according to the 148 region's of the Destrieux atlas with a 3mm isotropic Gaussian blur. The resting state fMRI data of 36 control subjects was decomposed into fifteen independent components nine of which resembled canonical resting state networks (Smith et al., 2009). These nine were subsequently projected into the same space as the Destrieux atlas. Regions exhibiting a mean z-score > 2.3 ($p < 0.01$) were entered into that network.

2.8 Defining resting state networks from functional imaging data

Independent component analysis (ICA) was used to separate the cortical resting state BOLD signals of the controls into independent components using FSL MELODIC. The optimal decomposition yielded fifteen components each representing a putative resting state network. The correlation of these components with the canonical networks identified by Smith et al. (2009) yielded nine behaviourally relevant resting state networks. These included regions associated with medial visual, occipital pole, dorsal attention, default mode, motor, auditory, salience, and fronto-parietal areas.

The nine independent components were subsequently projected onto the 148 regions of interest from the Destrieux atlas (Hellyer et al., 2014). A region was classified as belonging to a particular resting state network if its mean z-score was greater than 2.3 ($p < 0.01$). In detail, the z-scores contained within a given region's voxels were summed and divided by the total number of voxels in that region. If the mean z-score exceeded 2.3 ($p < 0.01$) that region was included in the resting state network. Figure 2 shows the nine canonical resting state networks reconstructed in MNI 152 space according to the 148 regions of the Destrieux atlas with a 3mm isotropic Gaussian blur.

2.9 Calculating resting state network metastability

Mean BOLD signals were subsequently transformed into complex phase representation via Hilbert transform. The first and last ten time points were removed to minimise border effects (Ponce-Alvarez et al., 2015). Oscillator phases were similarly extracted from the cortical network model. The Kuramoto order parameter (a measure of instantaneous synchronisation; Strogatz, 2000; Acebrón et al., 2005) was estimated for 1), the set of regions comprising single resting state network, and 2), when evaluating their interactions, the set of regions comprising two resting state networks, as:

$$R_{RSN}(t)=\frac{1}{N}\left|\sum_{k=1}^{N} e^{i\theta_K(t)}\right| \quad (1)$$

where $k=\{1,...,N\}$ is region number and $\theta_K(t)$ is the instantaneous phase of oscillator k at time t. Under complete independence, all phases are uniformly distributed and R_{RSN} approaches zero. Conversely, if all phases are equally distributed, R_{RSN} approaches one and full synchrony. Global metastability was calculated using all 148 cortical regions. The maintenance of a particular communication channel through coherence implies a

persistent phase relationship. The number or repertoire of such channels therefore corresponds to the variability of these phase relationships (i.e. the metastability) measured as the standard deviation of R_{RSN} (Kringelbach et al., 2015; Deco and Kringelbach, 2016).

2.10 Assessing connectivity changes between empirical resting state networks

Given that 1), the current formulation of metastability only permits calculation between a set of regions, and 2), that inter-connected subnetworks convey more behaviourally relevant information than single pairs of functional connectivity observed in isolation (Smith et al., 2009), we argue that an approach exploiting the clustering structure of connectivity alterations between functionally related networks may offer the optimal outcome in assessing connectivity changes between empirical resting state networks. Accordingly, we apply the NBS to measures of synchrony and metastability estimated from empirical fMRI data at the network rather than regional level.

The NBS is a non-parametric statistical test designed to deal with the multiple comparisons problem on a graph by identifying the largest connected sub-component (either increases or decreases) in topological space while controlling the family wise error rate (FWER). To date, several studies have used the method to identify pairwise regional connections that are associated with either an experimental effect or between-group difference in functional connectivity (Zalesky et al., 2010).

The present paper adopts a different approach. Rather than applying the NBS to a matrix of pairwise regional correlations, we apply the NBS to measures of synchrony and metastability evaluated at the resting state network level. Accordingly, pairwise interactions between all nine resting state networks were evaluated using the approach described above (see section 2.9). In the case of synchrony, we applied the NBS to 36 9x9 symmetric matrices derived from healthy controls and 34 9x9 symmetric matrices derived from subjects with AD. Of the matrices, each row/column represented an interaction between a resting state network and eight others. We performed the same procedure in the case of metastability. We report the mean synchrony and metastability of each group's interaction matrix in the supplementary information (Figs. S2 and S3).

First mass univariate testing is used to test the hypothesis of interest at every connection in the graph. Each connection is provided with a single test statistic capturing the evidence in favour of the null hypothesis, that is, there is no significant difference in the means of the two diagnostic groups (HC vs. MCI, HC vs. AD). Second, the test statistic is thresholded at

an arbitrary value. The set of connections exceeding this threshold are admitted into a set of supra-threshold connections representing potential candidates for which the null hypothesis can be rejected. The third step is to identify topological clusters among the supra-threshold connections for which a connected path can be found between any two nodes. It is important to note that clustering is not in physical space, rather the NBS clusters in topological space where a cluster corresponds to a connected graph component. The null hypothesis is therefore rejected or confirmed at the level of the whole structure rather than at the level of individual connections. The final step is to compute a FWER-corrected p-value for each component using permutation testing. For each permutation, the above three steps are repeated to construct an empirical null distribution of the largest connected component size. The FWER-corrected p-value for a component of a given size is estimated as the proportion of permutations for which the largest component was of the same size or greater. The size of a component can be measured in two ways 1) as the total number of connections or *extent* of that component or 2) as the sum of the test statistic values across all connections, namely, the *intensity* of that component. Extent is appropriate for detecting relatively weak effects that extend to encompass many connections while intensity is more suitable for detecting strong, focal effects confined to a limited number of connections. The threshold revealing the largest disconnected sub-component in the network was selected.

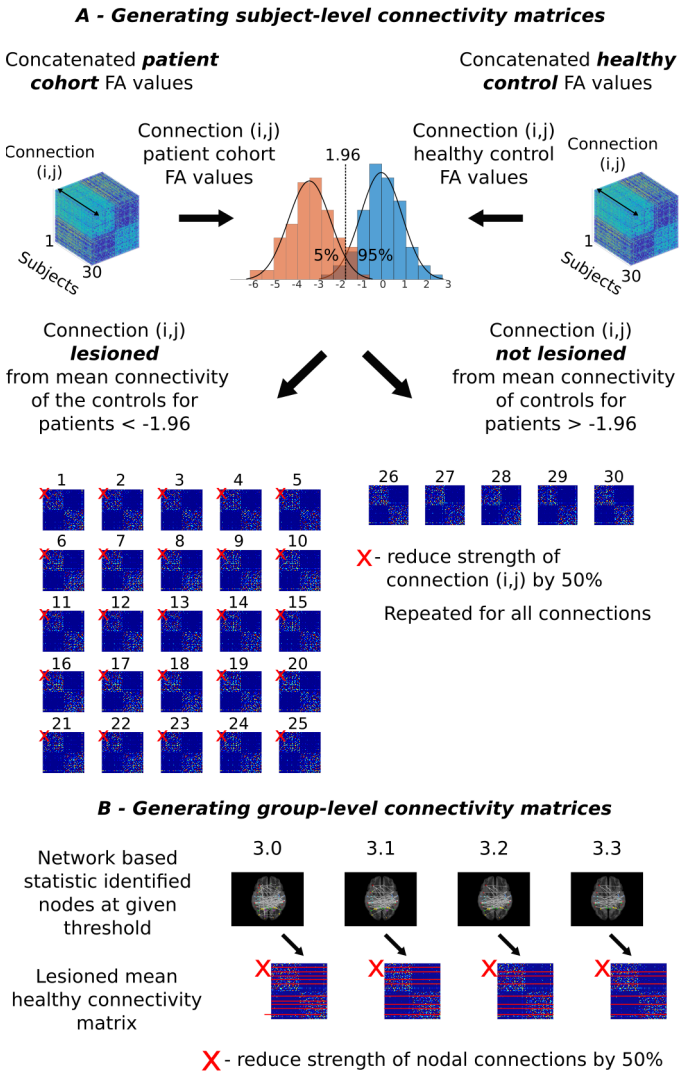

Figure 3: Estimation of subject-level structural disconnection in diagnostic groups (MCI/AD). A. Subject-level connectivity matrices were derived by lesioning the average control network or "healthy template" in locations where tracts demonstrated unusually low FA. The FA value for a single tract was extracted from all 30 controls to form a normal distribution with characteristic mean and standard deviation (blue). The same procedure in the patient cohort yielded a second normal distribution with a mean offset from the first (orange). Patients with tracts displaying FA values less than -1.96 standard deviations from the mean of the controls ($p < 0.05$; uncorrected) were considered damaged and lesioned from the average structural network of the controls, the strength of these connections being weakened by 50%. Repeating the procedure for all tracts yielded 30 subject-level connectivity matrices per diagnostic group (MCI/AD). B, Group-level structural connectivity matrices (MCI/AD) were derived for different values of the network based statistic threshold. Nodes forming part of significantly disconnected FA sub-components were considered damaged and lesioned from the average control network or "healthy template", the strength of these connections being weakened by 50%.

2.11 Generating subject-level structural connectivity

The derivation of structural connectivity relied on changes in FA which are more closely linked to axonal degeneration and demyelination (Aung et al., 2013; Teipel et al., 2014) than track count, which lacks a clear biological interpretation. Figure 3.A shows the procedure for generating subject-level connectivity matrices. Tracts demonstrating significantly lower FA than controls ($p < 0.05$; uncorrected) were lesioned from the healthy template i.e. the average structural connectivity of controls. This corresponded to a 5% probability that a control subject would exhibit an FA value this low. Since total denervation was unlikely, the strength of coupling was weakened by 50% with values ranging from 25-75% producing comparable results.

In detail, FA values $FA(i,j)$ of tracks running between pairwise regions i and j were concatenated for all 30 controls to form a 3D matrix $HC(i,j,k)$ of size $HC_{148\times148\times30}$. The same procedure was performed for the two patient cohorts to form $MCI(i,j,k)$ and $AD(i,j,k)$. The mean and standard deviation of the resulting normal distribution for $HC(i,j,*)$ was then used to convert FA values in the corresponding pairwise regions i and j of $MCI(i,j,*)$, and $AD(i,j,*)$ into z-values.

Comparison between the normal distribution of FA values for the tract (i,j) in the control population and the normal distribution of FA values for the tract (i,j) in the patient population was then possible. Patients were assigned their own copy of the healthy template prior to lesioning. Patients whose FA value was less than -1.96 standard deviations from the mean of the control FA distribution (corresponding to $p < 0.05$; uncorrected) had their tracts lesioned from the healthy template. The process was repeated for all tracts to produce 30 subject-level connectivity matrices in each patient cohort (MCI/AD).

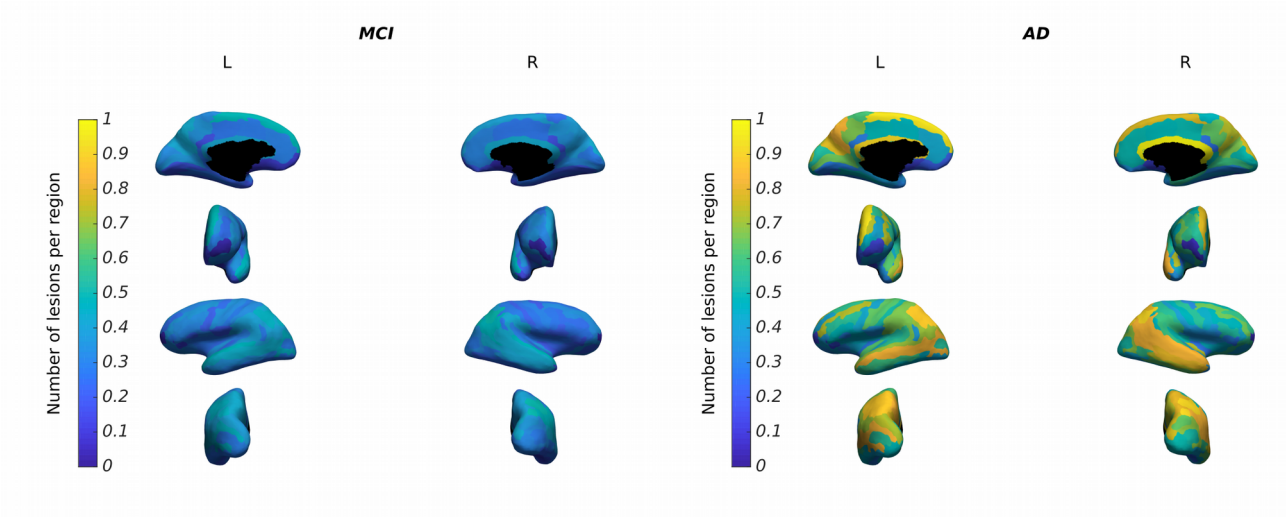

Figure 4: Total number of lesions pertaining to each region of the Destrieux cortical atlas in MCI (left) and AD cohorts (right), where blue indicates zero lesions and yellow the highest number recorded (normalised between zero and one). In both diagnostic groups, the majority of lesions was focused around core components of default mode network. Notice however the relative difference in magnitude.

2.12 Building a consensus distribution of structural lesions

The presence or absence of a lesioned tract was recorded in a binary matrix for each clinical subject. The summation of matrices within a diagnostic grouping yielded a single consensus distribution of lesioned tracts for all subjects where each index corresponded to the total number of subjects with a lesioned tract at that location (Fig. S1). Summing each row provided a regional measure corresponding to the total number of lesions in the connectivity of that region. Figure 4 shows this metric normalised between zero and one plotted on the inflated cortical surface of the Destrieux atlas where dark blue corresponds to zero lesions and yellow to the highest number recorded.

The purpose of the consensus distribution was three-fold: 1), to demonstrate how lesions were distributed on the cortical surface; 2), to determine which features of nodal topology were most associated with damage; and 3), to evaluate the distribution of lesions within the rich-club i.e. a network of high degree nodes that are more connected to each other than expected by chance (van den Heuvel and Sporns, 2011).

2.13 Generating group-level structural connectivity

Since networks grow or shrink in size depending on the choice of NBS threshold (note however the FWER is always controlled regardless of the choice of threshold) we employ a model-based fitting approach to determine the most likely structural skeleton (and hence threshold) responsible for generating the observed dynamic.

In this scenario, the NBS is used to guide the lesioning process. The resulting structure is used to inform coupling in the cortical network model. Firstly, the NBS identifies the largest disconnected sub-component in the FA matrix of the diagnostic group at a particular threshold. Secondly, the identified nodes are lesioned from the healthy template by having the strength of their connections reduced by 50%. Finally, the simulated dynamic (measured as resting state network synchrony and metastability) is correlated with empirical estimates based on fMRI BOLD signal (Figs. S2 and S3) allowing the most probable structural skeleton and hence most appropriate choice of threshold to be inferred. A control was provided by lesioning the same number of random nodes from the healthy template. Figure 3.B shows the procedure for generating group-level (MCI/AD) structural connectivity information at different values of the NBS threshold.

2.14 Constructing the cortical network model

The network model consisted of 148 nodes each described by a single Kuramoto phase oscillator (Kuramoto, 1984; Acebrón et al., 2005; Breakspear, 2017). Here, global synchronisation dynamics emerge through the reciprocal interaction of pairwise nodes coupled through the underlying anatomical structure. Despite its apparent simplicity, the Kuramoto model generates macroscopic dynamics comparable to significantly more complex spiking models at a significantly reduced computational cost (Messé et al., 2014).

The phase $\theta(t)$ of each oscillator i is governed by the equation:

$$\frac{d\theta_i}{dt} = \omega_i + \frac{1}{N}\sum_{j=1}^{N} K_{i,j}\sin\left(\theta_j - \theta_i - \rho\right) i = 1 \ldots N \quad (2)$$

where ω represents the oscillator's natural frequency i.e. the phase change of an uncoupled node per time step, N the total number of connections made by the oscillator, $K_{i,j}$ the strength of coupling between oscillators i and j , and ρ a fixed phase lag. In this context, phase lag is used as a ~~abstract~~ tuning parameter to match the simulated metastability to that of the empirical BOLD data (see: Computational model validation and tuning). Collective synchronisation between a set of oscillators can be achieved by increasing the coupling strength between the oscillating units, or by introducing a homogeneous distribution of frequencies between the oscillators. However, these strategies fail in the case where coupling between oscillators induces phase lags (Kundu et al., 2017). Such a scenario is common among many real-world systems (including the brain) where components take time to respond to their neighbouring oscillators. Under phase-frustration, the system indefinitely avoids synchronisation, even when frequencies are homogeneous and coupling is relatively strong. The phase lag parameter between oscillators can therefore be conceptualised as form of fixed time delay (Shanahan, 2010; Wildie and Shanahan, 2012). Metastable fluctuations in synchrony are only present for a critical range of the phase lag parameter. In this regime, integrative and segregative tendencies between oscillators are continually engaged but never fully reconciled.

The present paper simulates the BOLD signal directly using low frequency oscillators (Ponce-Alvarez et al., 2015). Such an approach should be distinguished from previous work where simulated electro-physiological signals (Hellyer et al., 2014, 2015; Váša et al., 2015) were transformed into BOLD signals using Balloon-Windkessel hemodynamics (Cabral et al., 2011, 2012). Since the match between simulated and empirical functional

connectivity is largely insensitive to the inclusion of hemodynamic effects (Messé et al., 2014), Balloon-Windkessel hemodynamics are not included here.

The oscillator's intrinsic frequency f_i and natural frequency ω_i are related through the equation $f_i = \omega_i / 2\pi$. The intrinsic frequencies are characterised as limit cycles distributed in the low frequency 0.04 – 0.07 Hz range of empirical BOLD signal oscillation. The model was numerically simulated in MATLAB 2016a (https://uk.mathworks.com) using the Runge-Kutta integration scheme with a time step of 10 ms. To ensure robust estimation of metastability and synchrony, we run the simulation for 1000 sec. with oscillator phase initialised randomly. We discard the first 200 sec. of simulation time to remove initial transients.

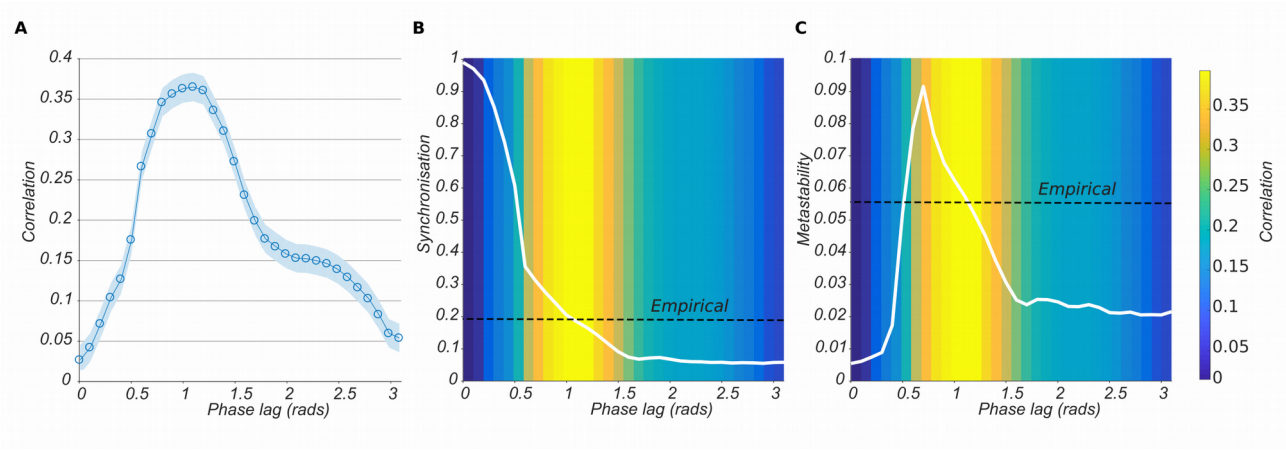

Figure 5: Model validation and tuning. A, Correlation between simulated and empirical functional connectivity for increasing value of phase lag parameter with 95% CI. B, Mean simulated global synchrony for increasing value of phase lag parameter with correlation overlaid for comparison. Correlation peaks where simulated synchronisation matches empirical synchronisation. C, Mean simulated global metastability for increasing value of phase lag parameter with correlation overlaid for comparison. Again, correlation peaks where simulated metastability matches empirical metastability.

2.16 Tuning and validating the cortical network model

Since empirical metastability intersected the curve of simulated metastability at two points and was thus, mathematically speaking, not a well defined function i.e. there were multiple values of phase lag that produced the same value of metastability, it alone was insufficient to tune the model. Instead, model validation and tuning was performed by correlating the average functional connectivity of the empirical BOLD data of healthy subjects with the average functional connectivity of the simulated cortical model over several runs at a given value of the phase lag parameter (Fig. 5.A). The value of phase lag producing the highest correlation (~1.1 rads) between simulated and empirical functional connectivity corresponded to the regime where empirical and simulated data agreed with each other (Fig. 5B, C; (Cabral et al., 2011, 2012, Hellyer et al., 2014, 2015; Váša et al., 2015). Pearson's correlation coefficients were calculated on pairwise BOLD signals to yield a functional connectivity matrix for each control subject. The mean functional connectivity of all controls was then calculated through simple averaging. Oscillator phase was transformed into a smooth periodic function representing BOLD signal, and Pearson's correlation coefficients were calculated between pairwise nodes of the model. One-hundred runs were conducted for different values of the phase lag parameter (0 to π) with the functional connectivity of each phase lag obtained through simple averaging. Oscillator phases were randomly initialised prior to each run and coupling between nodes informed by the average structural connectivity of the controls.

2.17 Evaluating the healthy structural connectome's local topology

The local topological organisation of each of the 148 nodes of the healthy template (i.e. the average structural network of the controls) were evaluated using the main graph theoretic measures (Bullmore and Sporns, 2009; Sporns, 2013). This included a measure of connectivity centrality – the eigenvector centrality. Under this framework, nodes have high eigenvector centrality if they have many neighbours, if their neighbours are highly connected or both). In other words, a node is important if it is linked by other important nodes. We also applied two local measures of segregation/integration – the clustering coefficient, or fraction of all possible edges linking a node's neighbours, and the local efficiency – the inverse average shortest path length between a node's neighbours. Finally, we applied a measure of modularity that relied upon an a priori definition of network modules or network components demonstrating high intra-connectivity but sparse inter-connectivity (see: Defining resting state networks from functional imaging data). These

included the participation coefficient, which captures how evenly a node's connections are distributed between modules. Metrics were evaluated using the Brain Connectivity Toolbox (Rubinov and Sporns, 2010). Full definitions are provided in the supplementary information.

2.18 Evaluating the lesioned structural connectome's large-scale topological organisation at the subject-level

We also evaluated four large-scale analogues of the previously described local measures namely, the mean eigenvector centrality, the mean clustering coefficient, global efficiency, and mean participation coefficient on the subject-level connectivity matrices. Three of these measures were discussed previously, the fourth – global efficiency – is closely related to path length and captures the trade-off between minimising network costs and maximising topological efficiency. For this reason, high global efficiency is associated with reduced wiring and metabolic costs, and faster, less noisy information transmission (Bullmore and Sporns, 2012). Again, a full definition is provided as supplementary information.

25

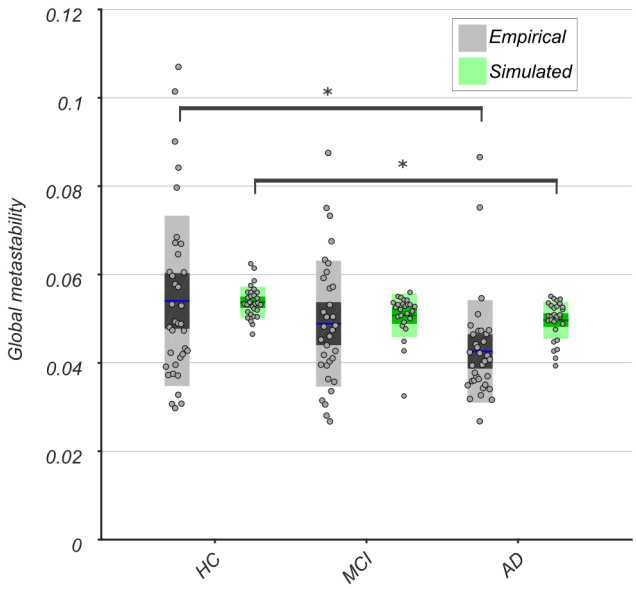

*Figure 6: Empirical global metastability of fMRI BOLD signal (in grey) and simulated global metastability (in green). Simulated metastability was calculated from a computer model with anatomically informed coupling. Empirical metastability was estimated from fMRI BOLD signal. Bars display mean, 95% CI, and one standard deviation for the three cohorts (HC/MCI/AD) with individual subjects indicated. One-way ANOVA revealed significantly lower metastability of large-scale neural dynamics in AD compared to controls for both empirical and simulated data (*p < 0.01).*

Results

3.1 Empirical estimates of large-scale neural metastability measured in fMRI BOLD signal are significantly reduced in AD

The metastability of the resting state fMRI BOLD signal was estimated for each cohort (Fig.6; in grey). Global metastability of healthy subjects declined asymptotically over the course of disease progression. One-way ANOVA identified a statistically significant difference between groups ($F(2,101) = 4.77$, $p = 0.011$). Subsequent Tukey post hoc test revealed significantly lower neural metastability in AD patients compared to controls ($p = 0.0073$).

3.2 Empirically defined macroscopic structural disconnection drives reduced metastability in large-scale simulations of neural dynamics

The impact of macroscopic structural disconnection on the large-scale neural dynamic was assessed by informing coupling between nodes in a simple oscillator model with subject-level connectivity data. Figure 6 shows the simulated metastability of each subject group (in green) compared to empirical estimates of global metastability (in grey).

Since the simulated results were contingent on the choice of starting parameters (the initial oscillator phases), we calculated the average global metastability produced from each subject's connectivity matrix over 100 runs (signified by a grey dot). For each run, a different set of initial oscillator phases was supplied. Each group (set of 30 subjects) received the same set of randomly initialised phases. Statistical tests were then conducted on the average values (the grey dots).

In agreement with empirical observations, simulated global metastability declined asymptotically according to diagnostic status. One-way ANOVA determined a statistically significant difference between groups ($F(59,88) = 7.83$, $p = 0.0007$). Subsequent Tukey post hoc test revealed significantly lower neural metastability in simulations informed by the subject-level connectivity matrices of AD patients compared to controls ($p = 0.00065$). Importantly, this result was robust against changes in the initial starting parameters (Fig. S4).

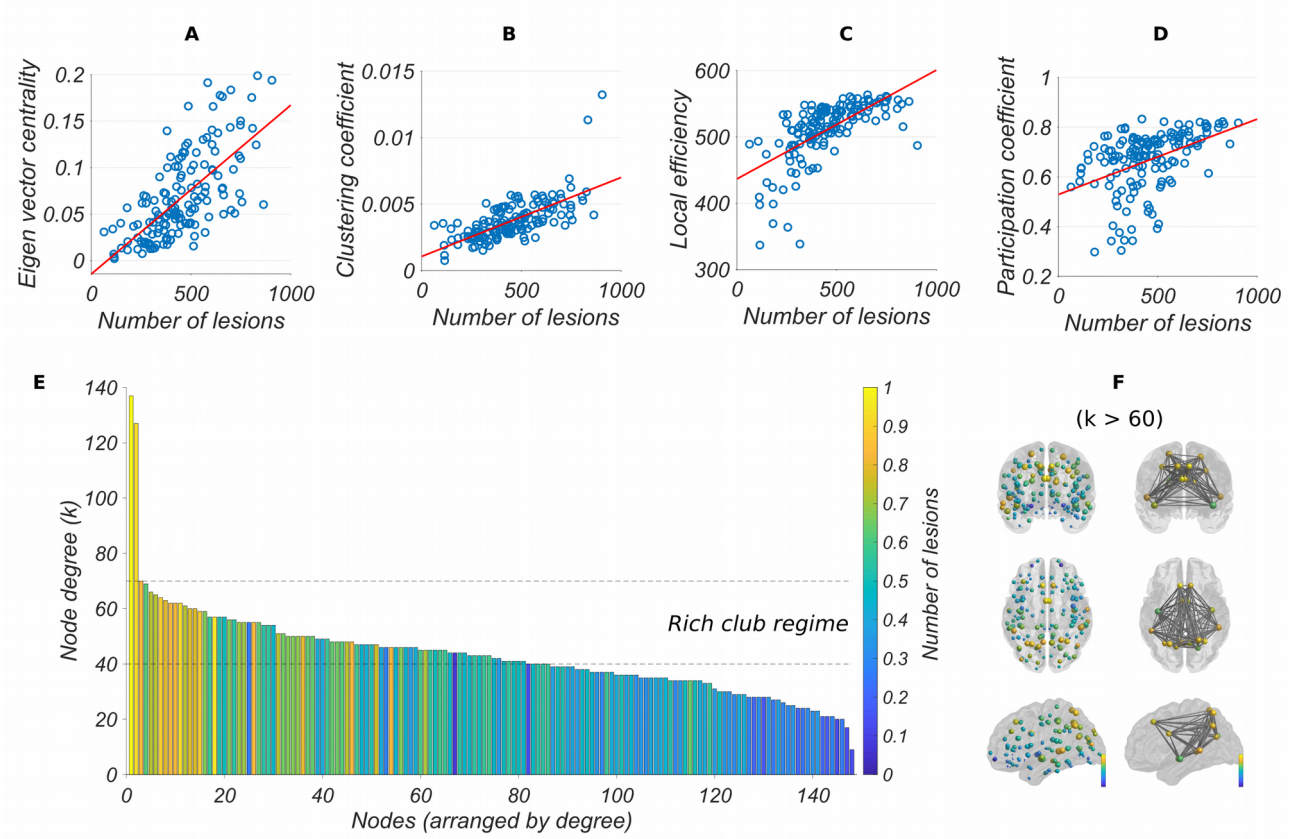

Figure 7: Local topological features of the average healthy connectome predict damage to nodal connectivity in the computer model (top) of AD subjects. This included A, eigenvector centrality, B, participation coefficient, C, clustering coefficient and D, local efficiency. All relationships were significant, corrected for multiple comparisons at the Bonferroni p-level of p < 0.001. Nodes of the rich club regime demonstrate the highest number of lesions (bottom). E, All 148 nodes of the Destrieux atlas rank ordered by degree with lesion count ranging from zero lesions, in blue, to the highest number recorded, in yellow, normalised to lie between zero and one. Dashed horizontal lines signal the rich-club regime between degrees = 40 and = 70. F, All 148 nodes of the Destrieux atlas plotted at the centre of mass of their respective cortical parcellations (left) with diameter proportional to degree and normalised lesion count indicated by colour. Nodes (and their edges) with degree > 60 qualifying for rich-club membership (right).

3.3 Local topological measures predict damage to the computer model's connectivity

Existing studies typically report finding significant differences in graph theoretic measures in clinical groups as compared controls (Tijms et al., 2013). However, here we relate the graph theoretic measure to the total number of lesions in the connectivity of each node. In doing so, we quantify the degree to which damage is correlated with specific features of the connectome's topology. Since strength of coupling between nodes is determined by subject-level connectome data, we emphasise that these results provide insight into how connectivity is damaged between nodes in the computer model. Accordingly, lesion count was entered into a linear regression analysis as dependent variable with one of four local graph metrics as predictors.

Patients demonstrated a statistically significant relationship between the number of lesions a node receives and key features of its structural topology, corrected for multiple comparisons at the Bonferroni p-level of $p < 0.001$. The relationship was more pronounced in the AD cohort.

For the MCI group, these included eigenvector centrality ($F(1,146) = 89.2$, $p = 8.17e\text{-}17$), clustering coefficient ($F(1,146) = 75.7$, $p = 6.26e\text{-}15$), local efficiency ($F(1,146) = 93.3$, $p = 2.24e\text{-}17$) and participation coefficient ($F(1,146) = 33.7$, $p = 3.87e\text{-}08$). For AD patients, these included eigenvector centrality ($F(1,146) = 125$, $p = 2.58e\text{-}21$), clustering coefficient ($F(1,146) = 124$, $p = 3.12e\text{-}21$), local efficiency ($F(1,146) = 106$, $p = 5.3e\text{-}19$) and participation coefficient ($F(1,146) = 35.1$, $p = 2.19e\text{-}08$).

Figure 7 (A-D) shows the total number of lesions in a node's connections plotted against the four measures of local topology. Since the results for the MCI group were qualitatively no different from AD, we present only the latter.

3.4 High-degree hubs of the rich-club are selectively vulnerability to damage

The human connectome is organised into a densely interconnected core of high-degree hub nodes known as the rich-club (van den Heuvel and Sporns, 2011). We investigated the relationship between a nodes rich-club membership and the total number of lesions within its connections.

Figure 7.E shows all 148 nodes rank ordered by degree with each node's normalised lesion count indicated by colour (ranging from zero lesions, blue, to the highest number of

lesions recorded, yellow) and dashed horizontal lines signalling the rich-club regime.

Figure 7.F (left) shows all nodes drawn at the centre of mass of their respective cortical parcellations, with diameter proportional to degree and normalised lesion count indicated by colour. For visualisation purposes, the diameter of the corpus callosum has been scaled to correspond to k = 70. Figure 7.F (right) shows those nodes and their edges with degree k > 60 that qualify for rich-club membership. As in previous work, a densely inter-connected core spanning multiple cortices and resting state networks is identified. These regions (and their respective resting state networks; see Fig. 2) included parieto-occipital sulcus (medial visual), intra-parietal sulcus (dorsal attention), precuneus and superior temporal sulcus (default mode), superior parietal lobule (default mode adjacent), inferior segment of the circular sulcus of the insula (auditory), and pericallosal sulcus of the corpus callosum (salience).

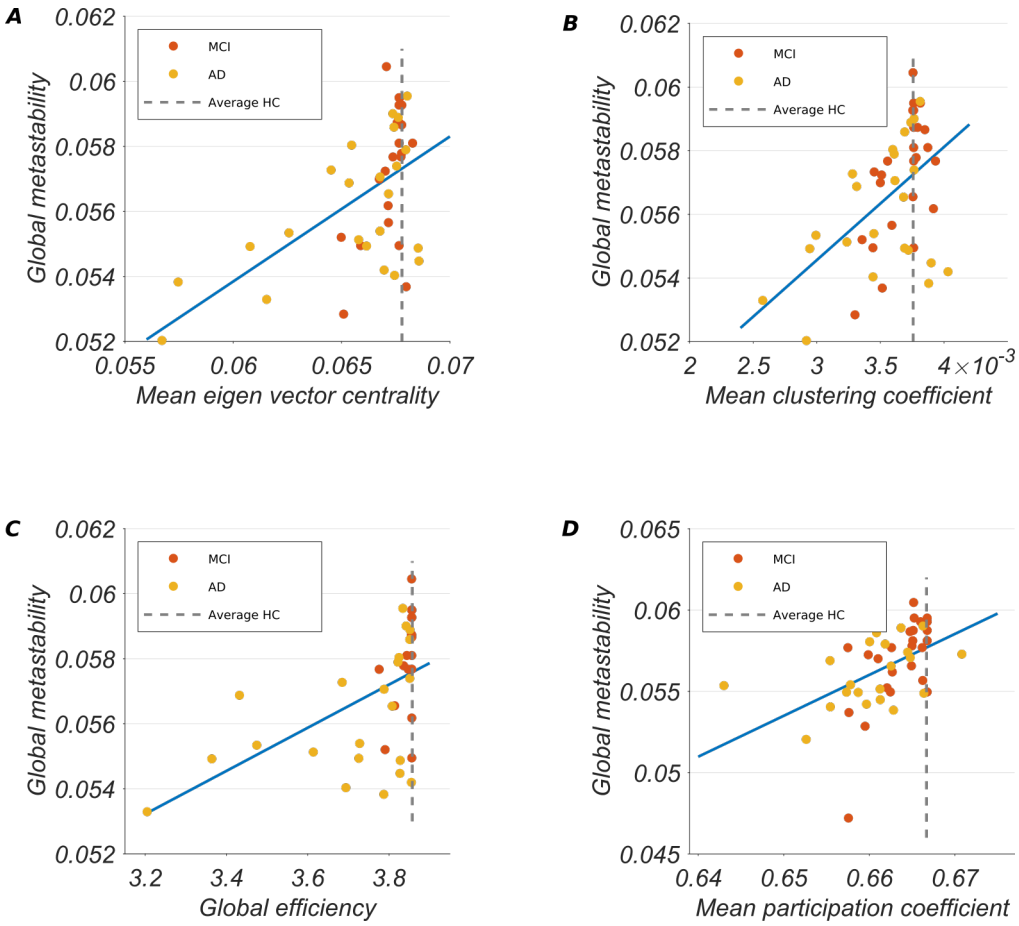

Figure 8: Relationship between macroscopic topological organisation including A, mean eigenvector centrality, B, mean clustering coefficient, C, global efficiency and D, mean participation coefficient after lesioning and simulated global metastability in MCI (in red) and AD cohorts (in yellow). A significant positive association was found between macroscopic measures of structural topology and simulated global metastability corrected for multiple comparisons at the Bonferroni p-level of $p < 0.0063$. For reference, vertical dashed line indicates the value obtained in the group-averaged control network.

3.5 Macroscopic topological organisation predicts simulated neural metastability

Simulated global metastability was entered into a linear regression analysis as dependent variable with large-scale graph theoretic measures of structural connectivity as predictors.

Since correlations could potentially be driven by a small number of extreme values, we removed outliers in the data prior to performing linear regression. We defined an outlier as an a value that is more than three scaled median absolute deviations away from the median. We perform this step for both the MCI and AD groups independently, and then perform a linear regression across all participants. Performing the regression with and without outliers did not qualitatively change the result.

Figure 8 shows the association between macroscopic topological organisation (after lesioning) and simulated global metastability. Both MCI and AD patients demonstrated a statistically significant relationship between simulated global metastability and the large-scale measures of structural topology, corrected for multiple comparisons at the Bonferroni p-level of $p < 0.0063$.

These included mean eigenvector centrality ($F(1,43) = 18.7$, $p = 0.00009$), mean clustering coefficient ($F(1,46 = 16.2$, $p = 0.0002$), global efficiency ($F(1,38) = 14.1$, $p = 0.0006$), and mean participation coefficient ($F(1,45) = 13.9$, $p = 0.00005$).

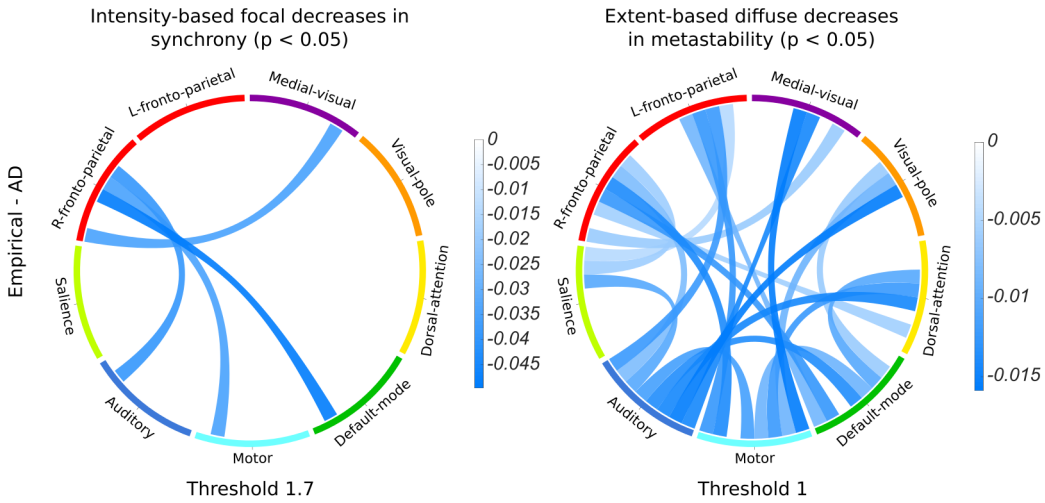

Figure 9: Statistically significant (p < 0.05; corrected) intensity-based decreases in focal synchrony between a circumscribed set of resting state networks identified using the network based statistic in fMRI data (left). Statistically significant (p < 0.05; corrected) extent-based decreases in metastability between a widespread set of resting state networks identified using the network based statistic in fMRI data (right). In both cases, the NBS was applied to matrices of synchrony and metastability calculated from empirical fMRI BOLD data at the resting state network level where thresholds were set to reveal the largest disconnected sub-graphs that were statistically significant.

3.6 Widespread decreases in metastability between empirical resting state networks in AD

We sought to identify network-level alterations in synchrony and metastability of resting state BOLD signal in the MCI and AD cohorts. Accordingly, we applied the NBS to the 9x9 matrices of synchrony and metastability estimated from empirical fMRI BOLD data for each subject (see section 2.10), where each row/column represented the interaction of a single resting state network with eight others.

The NBS identified statistically significant ($p = 0.033$; corrected) intensity-based focal decreases in synchrony between large-scale networks in AD. These included decreases between right fronto-parietal and sensory-motor networks, and between right fronto-parietal and default mode network.

The NBS also identified statistically significant ($p = 0.043$; corrected) extent-based decreases in metastability that subsumed all nine resting state networks in AD. Recall that extent is indicative of a relatively weak effect spread over many connections while intensity is associated with stronger effects confined to a small number of connections. No significant differences were identified in the MCI cohort for either synchrony ($p = 0.29$; corrected) or metastability ($p = 0.86$; corrected). Figure 9 shows the statistically significant sub-graphs ($p < 0.05$; corrected) of decreased synchrony (left) and metastability (right) identified by the NBS in the AD cohort.

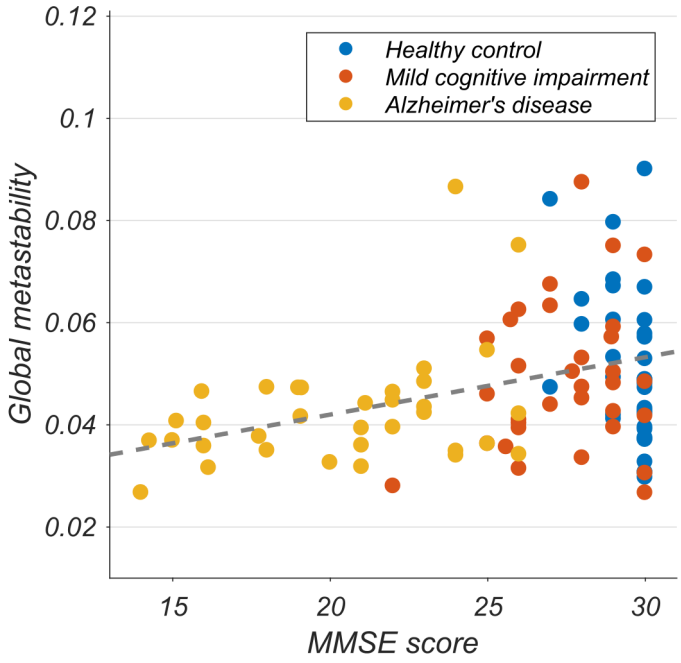

Figure 10: Relationship between global cognitive test scores and brain-wide metastability of fMRI BOLD signal. A significant association between global cognitive performance (MMSE) and empirical macroscopic neural metastability was found across all participants ($p < 0.01$).

3.7 Empirical measures of metastability predict cognitive performance in AD

To understand how empirical measures of neural metastability relate to cognitive performance, we performed a multiple linear regression with MMSE test score as dependent variable, global metastability as predictor, and age, motion, and total volume of grey matter as covariates of no interest. Figure 10 shows MMSE test score plotted against brain-wide metastability of empirical fMRI BOLD signal where each dot represents a single subject. A statistically significant association ($t(98) = 11.6$, $p = 0.0009$) was found between empirical measures of macroscopic neural metastability and cognitive performance across all subjects.

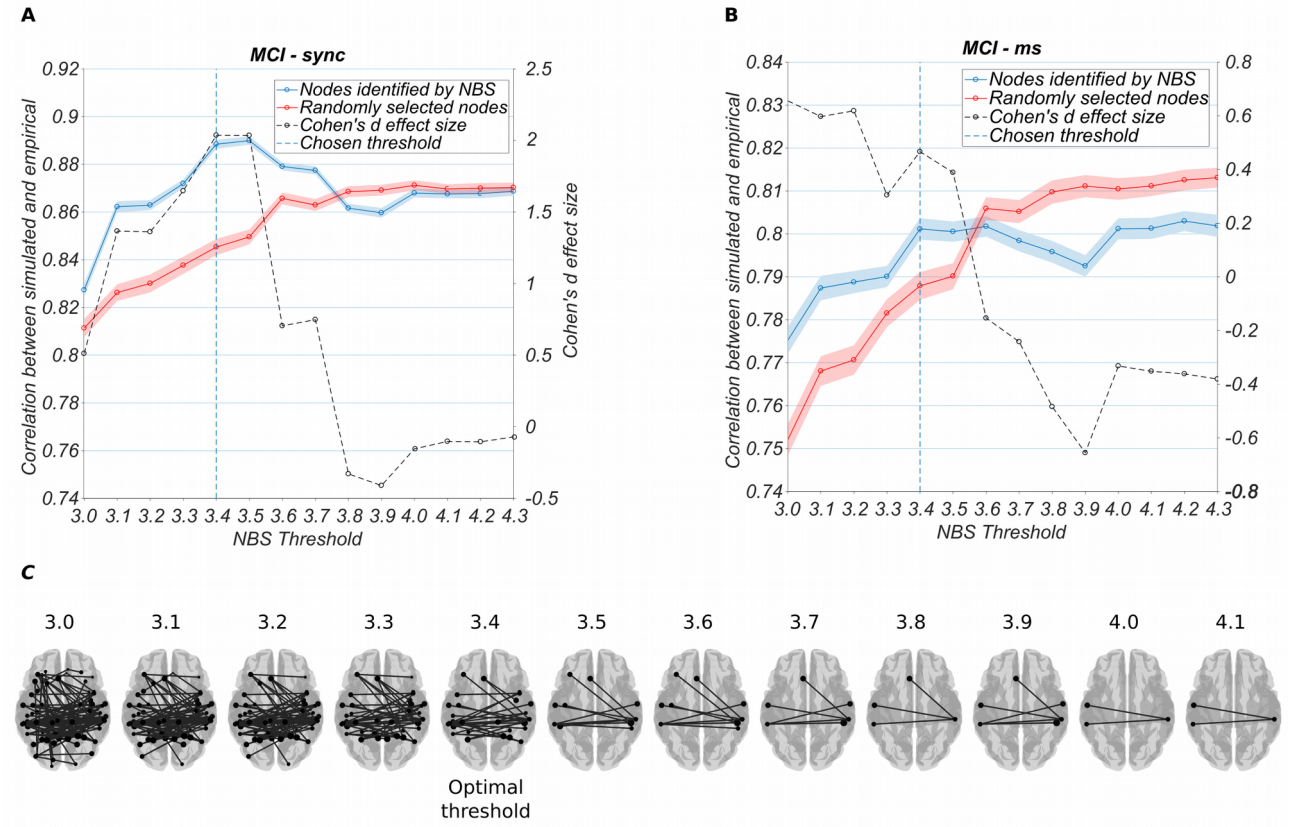

Figure 11. Determining the most likely group-level structural skeleton (or NBS threshold) responsible for generating the empirically observed resting state network synchronisation dynamic in the MCI cohort. A, Mean correlation between simulated synchrony (generated from a computer model with coupling defined by group-level connectivity) and empirical synchrony (measured in fMRI BOLD signal) drawn in blue with 95% CI. For comparison, the mean correlation between the simulated synchrony of a random control (generated from a computer model with randomly defined coupling) and empirical synchrony (measured in fMRI BOLD signal) is in red with 95% CI. Cohen's d effect size is indicated by black dashed line. The group-level connectivity or NBS threshold (3.4) at which correlation between simulated and empirical synchrony approximately peaked (r = 0.88) and the Cohen effect size maximised (d = 2.1). B, Same as in A but for metastability. At the group-level connectivity or NBS threshold of 3.4, correlations between simulated and empirical metastability are at their peak (r = 0.80) and the Cohen effect size is moderate (d = 0.5). C, Disconnected FA sub-networks identified by the NBS in a group of 30 patients with MCI at different thresholds (p < 0.05; corrected). Nodes are positioned at the centre of mass of their respective cortical parcellation. At each threshold, identified nodes had their connectivity lesioned from the average control connectivity. The resulting structure informed coupling strength between nodes in a group-level simulation.

870

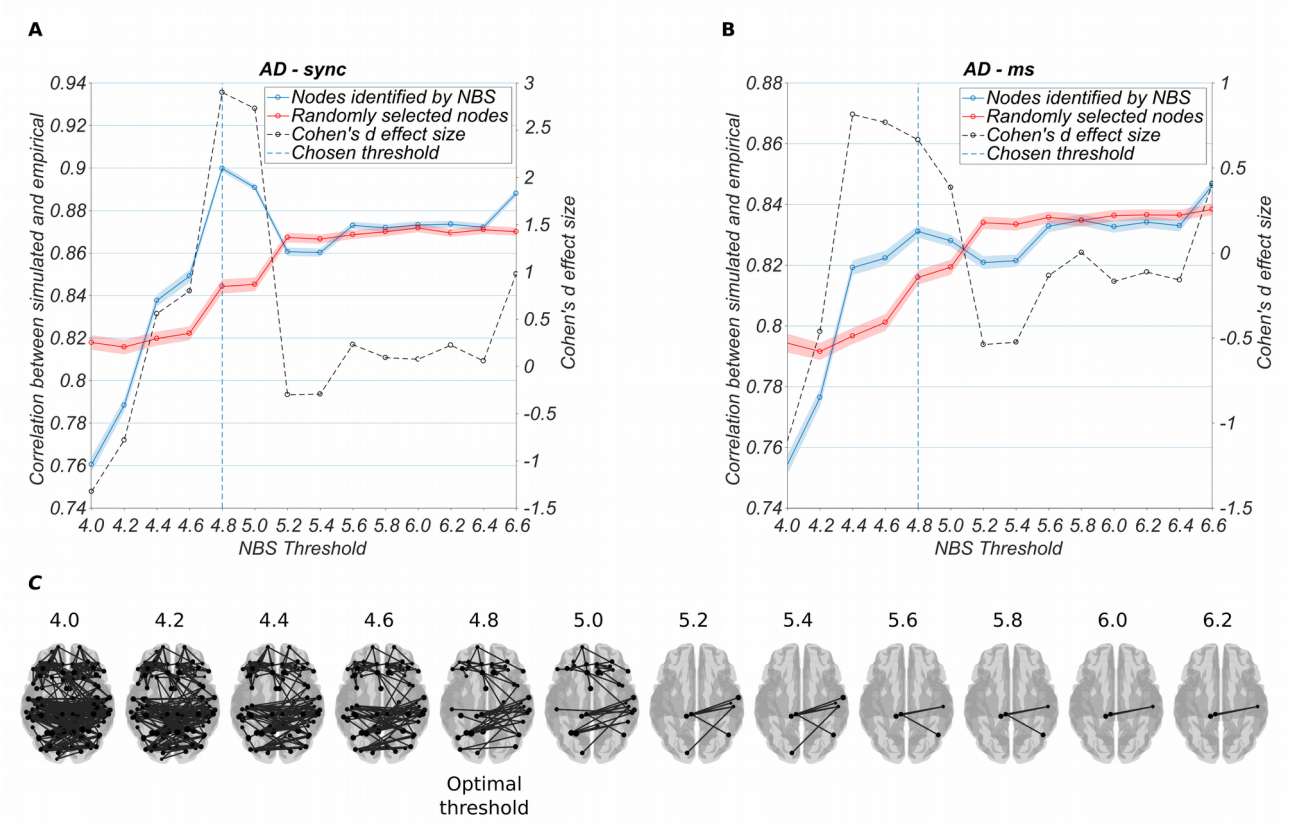

Figure 12. Determining the most likely group-level structural skeleton (or NBS threshold) responsible for generating the empirically observed resting state network synchronisation dynamic in the AD cohort. A, Mean correlation between simulated synchrony (generated from a computer model with coupling defined by group-level connectivity) and empirical synchrony (measured in fMRI BOLD signal) drawn in blue with 95% CI. For comparison, the mean correlation between the simulated synchrony of a random control (generated from a computer model with randomly defined coupling) and empirical synchrony (measured in fMRI BOLD signal) is in red with 95% CI. Cohen's d effect size is indicated by black dashed line. The group-level connectivity or NBS threshold (4.8) at which correlation between simulated and empirical synchrony approximately peaked (r = 0.9) and the Cohen effect size maximised (d = 2.9) was considered optimal. B, Same as in A but for metastability. At the group-level connectivity or NBS threshold of 4.8, correlations between simulated and empirical metastability are at their peak (r = 0.83) and the Cohen effect size is moderate (d = 0.75). C, Disconnected FA sub-networks identified by the NBS in a group of 30 patients with AD at different thresholds (p < 0.05; corrected). Nodes are positioned at the centre of mass of their respective cortical parcellation. At each threshold, identified nodes had their connectivity lesioned from the average control connectivity. The resulting structure informed coupling strength between nodes in a group-level simulation.

875

3.8 Dissociable networks of decreased FA identified in MCI and AD using dual NBS and model-based fitting approach

To identify the structural correlates underlying the observations of decreased synchrony between fronto-parietal and sensory-motor network in the AD cohort (Fig. 9), we invoked a joint model-based fitting and NBS procedure. In doing so, we identified dissociable networks of decreased FA between diagnostic groups. The AD cohort showed marked decreases in FA within portions of frontal and posterior cortex commensurate with fronto-parietal network. In contrast, the MCI cohort showed decreased FA in regions situated more centrally.

Figure 11.A shows the mean correlation between simulated synchrony (generated from the NBS identified structure) and mean empirical synchrony (measured using fMRI BOLD signal) in MCI patients drawn in blue with 95% CI. For comparison, the mean correlation between the simulated synchrony of a random control (generated by lesioning an equivalent number of random nodes) and mean empirical synchrony (measured using fMRI BOLD signal) is overlaid in red with 95% CI. We used Cohen's d effect size (indicated by black dashed line) to assess the standardised difference between the two means (blue and red) at different values of the NBS threshold.

The NBS threshold (3.4) at which correlation between simulated and empirical synchrony approximately peaked ($r = 0.88$; blue line) and the Cohen effect size was maximised ($d = 2.10$) is indicated by vertical dashed line. Two-sample t-test at the chosen threshold (3.4) revealed a statistically significant difference ($t(998) = 21.99$, $p < 0.01$; uncorrected) between 1) the mean correlations of the model informed by the group-level structure versus empirical fMRI data (blue), and 2) the mean correlations of the model informed by a randomly lesioned structure versus empirical fMRI data (red). Figures S2 and S3 show the correlation between simulated and empirical data at the chosen threshold.

Figure 11.B shows the mean correlation between simulated metastability (generated from the NBS identified structure) and empirical metastability (measured using fMRI BOLD signal) drawn in blue with 95% CI. Again, random controls are highlighted in red. At the chosen NBS threshold of 3.4, correlations between simulated and empirical metastability peaked ($r = 0.8$) and the Cohen effect size was moderate ($d = 0.5$). Two-sample t-test at this threshold (3.4) revealed a statistically significant difference ($t(998) = 6.38$, $p < 0.01$; uncorrected) between 1) the mean correlations of the model informed by the group-level

structure versus empirical fMRI data (blue) and 2) the mean correlations of the model informed by a randomly lesioned structure versus empirical fMRI data (red). Figure 11.C shows the disconnected FA sub-graph determined by the NBS ($p < 0.05$; corrected) for the MCI cohort at each threshold. The nodes identified at each threshold are listed in table S3. The nodes identified at the chosen threshold are shown in figure S7.

The same procedure was applied to the AD cohort. Figure 12.A shows the NBS threshold (4.8) at which correlation between simulated and empirical synchrony peaked ($r = 0.90$) and the Cohen effect size was maximised ($d = 2.9$) as vertical dashed line. Two-sample t-test at this threshold (4.8) revealed a statistically significant difference ($t(998) = 29.26$, $p < 0.01$; uncorrected) between 1) the mean correlations of the model informed by the NBS identified structure versus empirical fMRI data (blue), and 2) the mean correlations of the model informed by a randomly lesioned structure versus empirical fMRI data (red). Figures S2 and S3 show the correlation between simulated and empirical data at the chosen threshold.

Figure 12.B shows that at the chosen NBS threshold of 4.8, correlations between simulated and empirical metastability are close to their peak ($r = 0.83$; blue line) and the Cohen effect size is moderate ($d = 0.75$). Two-sample t-test at this threshold (4.8) revealed a statistically significant difference ($t(998) = 9.68$, $p < 0.01$; uncorrected) between 1) the mean correlations of the model informed by the NBS identified structure versus empirical fMRI data (blue) and 2) the mean correlations of the model informed by a randomly lesioned structure versus empirical fMRI data (red). Figure 12.C shows the disconnected FA sub-graph determined by the NBS ($p < 0.05$; corrected) for the AD cohort at each threshold. The nodes identified at each threshold are listed in table S4. The nodes identified at the chosen threshold are shown in figure S8.

Discussion

Structure, function, and cognition, can be arranged into an ontological triad each influencing the other. Interference to one component destabilises the triad, leading to measurable changes in the activity of the remaining two. This paper asked two broadly interrelated questions. How do higher level cognitive processes emerge from the interactions of dynamical networks of anatomically based brain connectivity, and how do disruptions to the topology of this structure impact network dynamics and ultimately

cognition? To answer these questions, we interrogated the neural dynamics of MCI and AD subjects for changes in metastability. In AD, macroscopic damage to the structural connectome produced reductions in simulated metastability comparable to that observed in empirical fMRI data (Fig. 6). Damage to the computer model's connectivity was focused around nodes scoring high in topological centrality, integration, and efficiency (Fig. 7). Reductions in simulated metastability were associated with damage to the connectome's global topology (Fig. 8). Brain-wide decreases in metastability contrasted sharply with more focal decreases in synchrony between resting state networks important for cognitive control (Fig. 9). Finally, the empirical decreases showed behavioural relevance, correlating with a subject's global cognitive ability (Fig. 10). Overall, the results of our dual computer modelling and empirical study suggest a causal relationship between metastability of neural dynamics, cognitive performance and the structural integrity of the human connectome.

We found reduced metastability in the global neural dynamic of fMRI BOLD signal in AD patients compared to healthy controls (Fig. 6). In a computer model informed by subject-level connectivity data, macroscopic structural disconnection was associated with reduced metastability of resting state neural dynamic in AD (Fig. 6) that matched similar declines in empirical data. Damage was selectively distributed according to the topological properties of each node in the healthy connectome (Fig. 7.A-D). Rich-club hubs (Fig. 7.E-F) and long distance, inter-modular tracts were especially vulnerable (Fig. S6). Reductions in simulated metastability correlated with damage to the structural connectome's large-scale topology (Fig. 8). Decreases in metastability were evident between most of the brain's resting state networks (Fig. 9). This is especially important in AD, as resting state networks are known to display a high degree of behavioural relevance (Smith et al., 2009). The level of neural metastability exhibited by a subject was related to the degree of behavioural impairment measured through cognitive testing (Fig. 10). These results lend further support to previous empirical observations of reduced cognitive flexibility and resting state neural metastability in conditions where network topology has been altered (Hellyer et al., 2015; Váša et al., 2015).

Eigenvector centrality correlated positively with damaged connectivity in the computer model (Fig. 7.A). Our findings are consistent with the selective vulnerability demonstrated by topologically important hub nodes in neurodegenerative disorders (Crossley et al., 2014). In AD, the elevated metabolism of default mode network hubs appears to convey a

greater risk of pathology (Buckner et al., 2009) – a view consistent with transgenic animal studies linking cellular activity to amyloid deposition (Cirrito et al., 2005; Bero et al., 2011) and simulations of activity dependent degeneration in hub regions (de Haan et al., 2012). Other hypotheses concerning the nature of brain network organisation and distribution of neuropathology have been proposed (Zhou et al., 2012). Foremost among these is the contention that pathology spreads transsynaptically in a prion-like manner between structurally and functionally related networks (Jaunmuktane et al., 2015). In support of this view, patterns of circumscribed atrophy are not randomly distributed with respect to the modular architecture of the brain. Rather, they appear to be constrained within specific resting state networks depending on the identity of the neurodegenerative disorder (Seeley et al., 2009). In keeping with this hypothesis, a relatively simple anatomically constrained diffusion process accurately predicted spatial patterns of neurodegeneration in AD (Raj et al., 2012). Our results indicate that pathological material is disseminated through the cortex by a network of nodes scoring high in eigenvector centrality.

Topologically integrated nodes with high clustering coefficient (Fig. 7.B) and local efficiency (Fig. 7.C) constituted a second locus of disruption in the computer model. Local network features providing tight integration between neighbouring nodes may facilitate the spread of pathological disease vectors within local communities (Raj et al., 2012). To date, disrupted clustering coefficient has been reported across imaging modalities in AD (Tijms et al., 2013).

Damage to the computer model's connectivity also correlated with a node's participation coefficient (Fig. 7.D). Nodes scoring high in participation coefficient bridge segregated communities by distributing their long range connections evenly between modules. Our results provide a physical basis for reports of reduced participation coefficient reported in functional connectivity networks in AD (Brier et al., 2014). Power et al. (2013) identified regions with high participation coefficient as convergence zones for different functional subsystems. Damage to these nodes produced much greater disruption in resting state organisation than lesions of equivalent magnitude in more circumscribed networks (Gratton et al., 2012). In another study, Warren et al.(2014) demonstrated that nodes with high participation played a distinct role from nodes of high degree. Crucially, lesions to nodes with high participation coefficient produced impairment across a range of cognitive domains, whereas lesions to high degree nodes displayed more circumscribed cognitive deficits. Such results are consistent with the finding of reduced integration between

network modules in our study and the global cognitive decline associated with AD. Furthermore, our results suggest a causal link between damage in high participation nodes, reduced metastability of neural dynamics, and decline in global cognitive performance.

Nodes demonstrating both high eigenvector centrality and high participation coefficient are likely part of the putative rich-club – a densely interconnected core of network hubs (van den Heuvel and Sporns, 2011; Pedersen and Omidvarnia, 2016). The rich-club phenomena occurs when hub nodes connect more densely among themselves than nodes of lower degree. Pathways linking these regions constitute an expensive high-performance backbone for global integration. Accordingly, the rich-club accounts for the majority of shortest paths between node pairs (van den Heuvel et al., 2012). Simulations show that targeted attack of rich-club hubs impair global efficiency three times more than randomly directed attacks (van den Heuvel et al., 2012). Our results show disrupted rich-club organisation across the AD spectrum with nodes of the rich-club regime demonstrating the greatest number of lesions in their connectivity (Fig. 7.E-F). In line with this view, reduced metastability may be a signature of disrupted rich-club organisation consistent with its role in boosting functional diversity (Senden et al., 2014).

The drive for rich-club architecture is associated with the tendency for hubs to connect regions over large physical distances (van den Heuvel et al., 2012). In a similar vein, cross modality sensory information is often integrated over long distances by hubs located in heteromodal association cortex. Damage to long distance association and commissural tracts (Fig. S6) may therefore provide an anatomical basis for reports of attenuated long range functional connectivity in AD (Liu et al., 2014).

Importantly, MMSE test scores correlated positively with empirical resting state global metastability in AD patients (Fig. 10). The MMSE measures the severity and progression of longitudinal cognitive impairment by testing abilities related to memory, attention, and language. All three domains involve the large-scale integration of information across distributed sensory, motor, and cognitive control regions. For this reason, metastability may represent an important mechanism underlying general cognitive function.

Our study found decreases in global metastability (Fig. 6) that correspond to an extended network of behaviourally relevant cognitive subsystems (Fig. 9). This is consistent with the understanding that higher order processes involving memory and attention (such as those

captured by the MMSE) are unlikely to reside within discrete topological modules. Instead, traditional modular architecture is likely dissolved in favour of a highly integrated global neuronal workspace (Dehaene et al., 1998). Measures of network integration including clustering coefficient, global efficiency, and participation coefficient, may therefore be more closely linked to higher order task performance than measures of segregation such as modularity (Bassett et al., 2011). In line with this view, reduced path length, heightened topological efficiency, and disrupted modular topology has been reported in functional networks during more challenging cognitive operations (Kitzbichler et al., 2011).

The present paper adopted a different strategy. Instead of assessing topological properties of functional connectivity networks directly, we used computer modelling to examine the link between a connectome's large-scale integrative structure and its ability to generate metastable neural dynamics. We did this by using anatomically derived subject-level connectivity data to inform coupling strength between nodes. With this approach, changes in metastable dynamic could be directly linked to topological changes taking place in the structural connectome. Since the subject-level connectomes were derived by lesioning the healthy template i.e. the average structural connectivity of the controls, the finding of reduced topological efficiency is perhaps unsurprising. Of note however, is the direct causal relationship between degraded topological structure and reduced metastability in the simulated neural dynamics. Crucially, in the present research, simulated and empirical data are in qualitative agreement (Fig. 6).

Overall, AD was defined by reduced connectivity between topologically important and well connected nodes, fragmented local network structure, increased path length between nodes, and reduced diversity of inter-module links. Accordingly, the structural connectomes belonging to MCI and AD subjects demonstrated a positive association between their simulated metastable dynamic and global measures of topological centrality, integration, and efficiency (Fig. 8.A-D). Such patterns of large-scale structural reorganisation may signal a shift in cost-efficiency trade-off in the direction of lowered metabolic costs at the price of reduced integrative capacity (Bullmore and Sporns, 2012).

Interestingly, time resolved fluctuations in resting state functional connectivity are characterised by two different states (Zalesky et al., 2014): one consistent with a long distance, highly efficient, integrated workspace configuration, and another, more segregated, less metabolically demanding configuration favouring local efficiency. The spontaneous switching of these configurations likely underlies the variation in synchrony

we registered here as metastability. On this basis, reduced metastability in AD may reflect a change in the transition rate or dwell time of each configuration (Jones et al., 2012). One hypothesis is that AD patients spend more time in segregated, locally efficient configurations and less time in metabolically demanding states of global integration. Thus, the indiscriminate decrease in brain-wide metastability observed in AD (Fig. 9) may signal a reduction in the brain's dynamic repertoire when subjects are at rest.

Diffuse decreases in metastability were accompanied by more circumscribed decreases in focal synchrony between fronto-parietal and sensory-motor network and between fronto-parietal and default mode network (Fig. 9). These decreases were consistent with structural damage in a comparable set of regions (Figs. 12.C and S8). The present results accord with recent findings of disrupted fronto-parietal network functional connectivity in AD (Zhao et al., 2018) and a growing consensus that frontal-parietal regions constitute a domain general control system for orchestrating more specialised networks (Vincent et al., 2008; Cole et al., 2013; Crossley et al., 2013). Recently, Dixon et al.(2018) revealed a novel processing stream between fronto-parietal and default mode network involved in regulating introspective behaviour. Of note are the associations between functions ascribed to the DMN and symptoms of AD. These include 1), recollection of autobiographical events in the past (Andreasen et al., 1995; Buckner and Carroll, 2007; Buckner et al., 2008); 2), simulation of prospective events and self-projection in the future (Schacter et al., 2007, 2008); and 3), theory of mind and social cognition (Schilbach et al., 2008; Spreng et al., 2009). Fronto-parietal and default mode network interactions have also been identified in autobiographical (Spreng et al., 2010) and working memory (Piccoli et al., 2015) that overlap with the core dysfunction of AD – the ability to author and recall one's own history (Gil et al., 2001). In fact, DMN dysfunction is considered a hallmark of incipient AD (Greicius et al., 2004). Tellingly, hypometabolism in default mode network structures has been found to correlate with anosognosia score in MCI patients (Therriault et al., 2018). The fronto-parietal control system has been proposed to play a central role in regulating mental health (Cole et al., 2014). Dubbed the "immune system of the mind" its flexible hubs may implement adaptive feedback control to regulate symptoms as they arise. Our results indicate a possible role for fronto-parietal network in default mode network dysfunction in AD.

Metastability is consistent with other descriptions of the brain as a dynamical system such as self-organised criticality (Hesse and Gross, 2014). For example, figure 5 implies a

phase transition from a highly disordered (sub-critical) to a highly ordered (super-critical) state. In finite systems such as the connectome, phase transitions do not occur at a precise point but are smoothed out over a parameter range (Tagliazucchi et al., 2012; Moretti and Muñoz, 2013). Thus, we find a small region between 0.5 and 1.5 rad that is not technically critical, but likely retains properties of criticality. These hallmarks of criticality lend critical systems their optimal information processing and storage capabilities (Shew and Plenz, 2013). Resting state dynamics of human brains demonstrate properties consistent with critical dynamics (Tagliazucchi et al., 2012). In this regime, the brain is likely poised at an equilibrium point of balanced excitation and inhibition where synchrony is maximally variable and pathological states of low or high synchrony are avoided (Yang et al., 2012). The consequences of highly variable synchrony on information processing is not well understood. Since the maintenance of a particular communication channel through coherence relies on a persistent phase relationship, the continuous variation in phase associated with metastability is potentially commensurate with a large number of independent communication channels (Deco and Kringelbach, 2016).

Some limitations should be noted. Since there are many ways of defining a network both functionally and structurally, and at multiple scales, the current results are only valid for the Destrieux atlas parcellation. Since the major sulci and gyri are unlikely to align well with functional activity, future modelling work may benefit from using atlas regions defined multi-modally, that is, based on more than one neurobiological property (Glasser et al., 2016). In addition, the use of model-based fitting to select the structural skeleton responsible for generating the observed dynamic does not consider likely degeneracies in the structural data i.e. the method only considers a subset of the possible structural lesions responsible for changes in empirical metastability. Any lesions outside the largest detected component are explicitly ignored.

In summary, we used a neurodegenerative disorder, AD, and its prodromal stage MCI, to clarify the relationship between structural network topology and metastable neural dynamics. Overall, our results indicate a causal relationship between structure, dynamics, and cognition and support the contention that structure and cognition can be bridged through metastability (Kelso, 1995, 2012, Tognoli and Kelso, 2009, 2014a, 2014b). In AD, metastability of fMRI BOLD signal was decreased and this correlated with cognitive performance. Using a model based on empirical connectivity we showed a direct link between reductions in metastability and structural damage. These findings offer a distinct

perspective on the network-level role of metastability in cognition, its relation to structure, and its inexorable decline in neurodegenerative disease.

Acknowledgements

This work was supported by a Department for Employment and Learning Northern Ireland PhD studentship. This work was also supported, in part, by a grant given to ALWB from Science Foundation Ireland (grant number 11/RFP.1/NES/3194). JASK is supported by a grant from the National Institute of Mental Health (MH080838), the Chaire d'Excellence Pierre de Fermat, and the Davimos Family Endowment for Excellence in Science.

Data collection and sharing for this project were funded by the Alzheimer's Disease Neuroimaging Initiative (ADNI) (National Institutes of Health Grant U01 AG024904) and DOD ADNI (Department of Defense award number W81XWH-12-2-0012). ADNI is funded by the National Institute on Aging, the National Institute of Biomedical Imaging and Bioengineering, and through generous contributions from the following: AbbVie,

Alzheimer's Association; Alzheimer's Drug Discovery Foundation; Araclon Biotech; BioClinica, Inc.; Biogen; Bristol-Myers Squibb Company; CereSpir, Inc.; Cogstate; Eisai Inc.; Elan Pharmaceuticals, Inc.; Eli Lilly and Company; EuroImmun; F. Hoffmann-La Roche Ltd and its affiliated company Genentech, Inc.; Fujirebio; GE Healthcare; IXICO Ltd.; Janssen Alzheimer Immunotherapy Research & Development, LLC.; Johnson & Johnson Pharmaceutical Research & Development LLC.; Lumosity; Lundbeck; Merck & Co., Inc.; Meso Scale Diagnostics, LLC.; NeuroRx Research; Neurotrack Technologies; Novartis Pharmaceuticals Corporation; Pfizer Inc.; Piramal Imaging; Servier; Takeda Pharmaceutical Company; and Transition Therapeutics. The Canadian Institutes of Health Research is providing funds to support ADNI clinical sites in Canada. Private sector contributions are facilitated by the Foundation for the National Institutes of Health (www.fnih.org). The grantee organization is the Northern California Institute for Research and Education, and the study is coordinated by the Alzheimer's Therapeutic Research Institute at the University of Southern California. ADNI data are disseminated by the Laboratory for Neuro Imaging at the University of Southern California.

Bibliography

Acebrón, J. a., Bonilla, L.L., Vicente, C.J.P., Ritort, F., Spigler, R., 2005. The Kuramoto model: A simple paradigm for synchronization phenomena. Rev. Mod. Phys. 77, 137–185. https://doi.org/10.1103/RevModPhys.77.137

Andersson, J.L.R., Jenkinson, M., Smith, S., 2007. Non-linear registration aka Spatial normalisation FMRIB Technial Report TR07JA2, In Practice.

Andreasen, N.C., O'Leary, D.S., Cizadlo, T., Arndt, S., Rezai, K., Watkins, G.L., Ponto, L.L.B., Hichwa, R.D., 1995. Remembering the past: Two facets of episodic memory explored with positron emission tomography. Am. J. Psychiatry 152, 1576–1585. https://doi.org/10.1176/ajp.152.11.1576

Aung, W.Y., Mar, S., Benzinger, T.L., 2013. Diffusion tensor MRI as a biomarker in axonal and myelin damage. Imaging Med. 5, 427–440. https://doi.org/10.2217/iim.13.49

Bassett, D.S., Wymbs, N.F., Porter, M.A., Mucha, P.J., Carlson, J.M., Grafton, S.T., 2011. Dynamic reconfiguration of human brain networks during learning. Proc. Natl. Acad. Sci. U. S. A. 108, 7641–6. https://doi.org/10.1073/pnas.1018985108

Bero, A.W., Yan, P., Roh, J.H., Cirrito, J.R., Stewart, F.R., Raichle, M.E., Lee, J.M., Holtzman, D.M., 2011. Neuronal activity regulates the regional vulnerability to amyloid-beta deposition. Nat. Neurosci. 14, 750–756. https://doi.org/10.1038/nn.2801

Braak, E., Griffing, K., Arai, K., Bohl, J., Bratzke, H., Braak, H., 1999. Neuropathology of Alzheimer's disease: what is new since A. Alzheimer? Eur. Arch. Psychiatry Clin. Neurosci. 249 Suppl, 14–22. https://doi.org/10.1007/PL00014168

Braak, H., Braak, E., 1991. Neuropathological stageing of Alzheimer-related changes. Acta Neuropathol. 82, 239–259. https://doi.org/10.1007/BF00308809

Breakspear, M., 2017. Dynamic models of large-scale brain activity. Nat. Neurosci. https://doi.org/10.1038/nn.4497

Bressler, S.L., Kelso, J.A.S., 2016. Coordination Dynamics in Cognitive Neuroscience. Front. Neurosci. 10, 397. https://doi.org/10.3389/fnins.2016.00397

Bressler, S.L., Kelso, J.A.S., 2001. Cortical coordination dynamics and cognition. Trends Cogn. Sci. https://doi.org/10.1016/S1364-6613(00)01564-3

Brier, M.R., Thomas, J.B., Ances, B.M., 2014. Network dysfunction in Alzheimer's disease: refining the disconnection hypothesis. Brain Connect. 4, 299–311. https://doi.org/10.1089/brain.2014.0236

Brun, A., Englund, E., 1986. A white matter disorder in dementia of the Alzheimer type: A pathoanatomical study. Ann. Neurol. 19, 253–262. https://doi.org/10.1002/ana.410190306

Buckner, R.L., Andrews-Hanna, J.R., Schacter, D.L., 2008. The brain's default network: anatomy, function, and relevance to disease. Ann. N. Y. Acad. Sci. 1124, 1–38. https://doi.org/10.1196/annals.1440.011

Buckner, R.L., Carroll, D.C., 2007. Self-projection and the brain. Trends Cogn. Sci. 11, 49–57. https://doi.org/10.1016/j.tics.2006.11.004

Buckner, R.L., Sepulcre, J., Talukdar, T., Krienen, F.M., Liu, H., Hedden, T., Andrews-Hanna, J.R., Sperling, R. a, Johnson, K. a, 2009. Cortical hubs revealed by intrinsic functional connectivity: mapping, assessment of stability, and relation to Alzheimer's disease. J. Neurosci. 29, 1860–73. https://doi.org/10.1523/JNEUROSCI.5062-08.2009

Buckner, R.L., Snyder, A.Z., Shannon, B.J., LaRossa, G., Sachs, R., Fotenos, A.F., Sheline, Y.I., Klunk, W.E., Mathis, C. a, Morris, J.C., Mintun, M. a, 2005. Molecular, structural, and functional characterization of Alzheimer's disease: evidence for a relationship between default activity, amyloid, and memory. J. Neurosci. 25, 7709–17. https://doi.org/10.1523/JNEUROSCI.2177-05.2005

Bullmore, E., Sporns, O., 2012. The economy of brain network organization. Nat. Rev. Neurosci. 13, 336–49. https://doi.org/10.1038/nrn3214

Bullmore, E., Sporns, O., 2009. Complex brain networks: Graph theoretical analysis of structural and functional systems. Nat. Rev. Neurosci. 10, 186–198. https://doi.org/10.1038/nrn2575

Cabral, J., Hugues, E., Kringelbach, M.L., Deco, G., 2012. Modeling the outcome of structural disconnection on resting-state functional connectivity. Neuroimage 62, 1342–1353. https://doi.org/10.1016/j.neuroimage.2012.06.007

Cabral, J., Hugues, E., Sporns, O., Deco, G., 2011. Role of local network oscillations in resting-state functional connectivity. Neuroimage 57, 130–9. https://doi.org/10.1016/j.neuroimage.2011.04.010

Cabral, J., Kringelbach, M.L., Deco, G., 2014. Exploring the network dynamics underlying brain activity during rest. Prog. Neurobiol. 114, 102–131. https://doi.org/10.1016/j.pneurobio.2013.12.005

Cirrito, J.R., Yamada, K. a., Finn, M.B., Sloviter, R.S., Bales, K.R., May, P.C., Schoepp, D.D., Paul, S.M., Mennerick, S., Holtzman, D.M., 2005. Synaptic activity regulates interstitial fluid amyloid-beta levels in vivo. Neuron 48, 913–922. https://doi.org/10.1016/j.neuron.2005.10.028

Cole, M.W., Repovš, G., Anticevic, A., 2014. The frontoparietal control system: a central role in mental health. Neuroscientist 20, 652–64. https://doi.org/10.1177/1073858414525995

Cole, M.W., Reynolds, J.R., Power, J.D., Repovs, G., Anticevic, A., Braver, T.S., 2013. Multi-task connectivity reveals flexible hubs for adaptive task control. Nat. Neurosci. 16, 1348–55. https://doi.org/10.1038/nn.3470

Córdova-Palomera, A., Kaufmann, T., Persson, K., Alnæs, D., Doan, N.T., Moberget, T., Lund, M.J., Barca, M.L., Engvig, A., Brækhus, A., Engedal, K., Andreassen, O.A., Selbæk, G., Westlye, L.T., 2017. Disrupted global metastability and static and dynamic brain connectivity across individuals in the Alzheimer's disease continuum. Sci. Rep. 7, 40268. https://doi.org/10.1038/srep40268

Crossley, N.A., Mechelli, A., Vertes, P.E., Winton-Brown, T.T., Patel, A.X., Ginestet, C.E., McGuire, P., Bullmore, E.T., 2013. Cognitive relevance of the community structure of the human brain functional coactivation network. Proc. Natl. Acad. Sci. 110, 11583–11588. https://doi.org/10.1073/pnas.1220826110

Crossley, N. a., Mechelli, a., Scott, J., Carletti, F., Fox, P.T., McGuire, P., Bullmore, E.T., 2014. The hubs of the human connectome are generally implicated in the anatomy of brain disorders. Brain 2117–2118. https://doi.org/10.1093/brain/awu132

Damoiseaux, J.S., Rombouts, S.A.R.B., Barkhof, F., Scheltens, P., Stam, C.J., Smith, S.M., Beckmann, C.F., 2006. Consistent resting-state networks across healthy subjects. Proc. Natl. Acad. Sci. U. S. A. 103, 13848–53. https://doi.org/10.1073/pnas.0601417103

de Haan, W., Mott, K., van Straaten, E.C.W., Scheltens, P., Stam, C.J., 2012. Activity dependent degeneration explains hub vulnerability in Alzheimer's disease. PLoS Comput. Biol. 8, e1002582. https://doi.org/10.1371/journal.pcbi.1002582

de la Monte, S.M., 1989. Quantitation of cerebral atrophy in preclinical and end□stage alzheimer's disease. Ann. Neurol. 25, 450–459. https://doi.org/10.1002/ana.410250506

Deco, G., Jirsa, V., McIntosh, A.R., Sporns, O., Kötter, R., 2009. Key role of coupling, delay, and noise in resting brain fluctuations. Proc. Natl. Acad. Sci. U. S. A. 106, 10302–7. https://doi.org/10.1073/pnas.0901831106

Deco, G., Jirsa, V.K., 2012. Ongoing Cortical Activity at Rest: Criticality, Multistability, and Ghost Attractors. J. Neurosci. 32, 3366–3375. https://doi.org/10.1523/JNEUROSCI.2523-11.2012

Deco, G., Jirsa, V.K., McIntosh, A.R., 2013a. Resting brains never rest: Computational insights into potential cognitive architectures. Trends Neurosci. 36, 268–274. https://doi.org/10.1016/j.tins.2013.03.001

Deco, G., Kringelbach, M.L., 2016. Metastability and Coherence: Extending the Communication through Coherence Hypothesis Using A Whole-Brain Computational Perspective. Trends Neurosci. https://doi.org/10.1016/j.tins.2016.01.001

Deco, G., Kringelbach, M.L., 2014. Great expectations: Using whole-brain computational connectomics for understanding neuropsychiatric disorders. Neuron. https://doi.org/10.1016/j.neuron.2014.08.034

Deco, G., Ponce-Alvarez, A., Mantini, D., Romani, G.L., Hagmann, P., Corbetta, M., 2013b. Resting-State Functional Connectivity Emerges from Structurally and Dynamically Shaped Slow Linear Fluctuations. J. Neurosci. 33, 11239–11252. https://doi.org/10.1523/JNEUROSCI.1091-13.2013

Deco, G., Tononi, G., Boly, M., Kringelbach, M.L., 2015. Rethinking segregation and integration: contributions of whole-brain modelling. Nat. Rev. Neurosci. 16, 430–9. https://doi.org/10.1038/nrn3963

Dehaene, S., Kerszberg, M., Changeux, J.-P., 1998. A neuronal model of a global workspace in effortful cognitive tasks. Proc. Natl. Acad. Sci. 95, 14529–14534. https://doi.org/10.1073/pnas.95.24.14529

Demirtaş, M., Falcon, C., Tucholka, A., Gispert, J.D., Molinuevo, J.L., Deco, G., 2017. A whole-brain computational modeling approach to explain the alterations in resting-state functional connectivity during progression of Alzheimer's disease. NeuroImage Clin. 16, 343–354. https://doi.org/10.1016/j.nicl.2017.08.006

Desai, M.K., Mastrangelo, M.A., Ryan, D.A., Sudol, K.L., Narrow, W.C., Bowers, W.J., 2010. Early oligodendrocyte/myelin pathology in Alzheimer's disease mice constitutes a novel therapeutic target. Am. J. Pathol. 177, 1422–35. https://doi.org/10.2353/ajpath.2010.100087

Desai, M.K., Sudol, K.L., Janelsins, M.C., Mastrangelo, M.A., Frazer, M.E., Bowers, W.J., 2009. Triple-transgenic Alzheimer's disease mice exhibit region-specific abnormalities in brain myelination patterns prior to appearance of amyloid and tau pathology. Glia 57, 54–65. https://doi.org/10.1002/glia.20734

Desikan, R.S., Ségonne, F., Fischl, B., Quinn, B.T., Dickerson, B.C., Blacker, D., Buckner, R.L., Dale, A.M., Maguire, R.P., Hyman, B.T., Albert, M.S., Killiany, R.J., 2006. An automated labeling system for subdividing the human cerebral cortex on MRI scans into gyral based regions of interest. Neuroimage 31, 968–980. https://doi.org/10.1016/j.neuroimage.2006.01.021

Dixon, M.L., De La Vega, A., Mills, C., Andrews-Hanna, J., Spreng, R.N., Cole, M.W., Christoff, K., 2018. Heterogeneity within the frontoparietal control network and its relationship to the default and dorsal attention networks. Proc. Natl. Acad. Sci. 115, E1598–E1607. https://doi.org/10.1073/pnas.1715766115

Engstrøm, D.A., Scott Kelso, J., 2008. Coordination Dynamics of the Complementary Nature. Gestalt Theory 30, 121–134. https://doi.org/10.1016/j.neuropsychologia.2008.05.019

Fischl, B., Liu, A., Dale, A.M., 2001. Automated manifold surgery: Constructing geometrically accurate and topologically correct models of the human cerebral cortex. IEEE Trans. Med. Imaging 20, 70–80. https://doi.org/10.1109/42.906426

Fischl, B., Salat, D.H., Busa, E., Albert, M., Dieterich, M., Haselgrove, C., Van Der Kouwe, A., Killiany, R., Kennedy, D., Klaveness, S., Montillo, A., Makris, N., Rosen, B., Dale, A.M., 2002. Whole brain segmentation: Automated labeling of neuroanatomical structures in the human brain. Neuron 33, 341–355. https://doi.org/10.1016/S0896-6273(02)00569-X

Fischl, B., Salat, D.H., Van Der Kouwe, A.J.W., Makris, N., Ségonne, F., Quinn, B.T., Dale, A.M., 2004a. Sequence-independent segmentation of magnetic resonance images, in: NeuroImage. https://doi.org/10.1016/j.neuroimage.2004.07.016

Fischl, B., Van Der Kouwe, A., Destrieux, C., Halgren, E., Ségonne, F., Salat, D.H., Busa, E., Seidman, L.J., Goldstein, J., Kennedy, D., Caviness, V., Makris, N., Rosen, B., Dale, A.M., 2004b. Automatically Parcellating the Human Cerebral Cortex. Cereb. Cortex 14, 11–22. https://doi.org/10.1093/cercor/bhg087

Folstein, M.F., Folstein, S.E., McHugh, P.R., 1975. “Mini-mental state.” J. Psychiatr. Res. 12, 189–198. https://doi.org/10.1016/0022-3956(75)90026-6

Ghosh, A., Rho, Y., McIntosh, A.R., Kötter, R., Jirsa, V.K., 2008. Cortical network dynamics with time delays reveals functional connectivity in the resting brain. Cogn. Neurodyn. 2, 115–20. https://doi.org/10.1007/s11571-008-9044-2

Gil, R., Arroyo-Anllo, E.M., Ingrand, P., Gil, M., Neau, J.P., Ornon, C., Bonnaud, V., 2001. Self-consciousness and Alzheimer’s disease. Acta Neurol. Scand. 104, 296–300. https://doi.org/10.1034/j.1600-0404.2001.00280.x

Glasser, M.F., Coalson, T.S., Robinson, E.C., Hacker, C.D., Harwell, J., Yacoub, E., Ugurbil, K., Andersson, J., Beckmann, C.F., Jenkinson, M., Smith, S.M., Van Essen, D.C., 2016. A multi-modal parcellation of human cerebral cortex. Nature 536, 171–8. https://doi.org/10.1038/nature18933

Glerean, E., Salmi, J., Lahnakoski, J.M., Jaaskelainen, I.P., Sams, M., 2012. Functional magnetic resonance imaging phase synchronization as a measure of dynamic functional connectivity. Brain Connect 2, 91–101. https://doi.org/10.1089/brain.2011.0068

Gratton, C., Nomura, E.M., Pérez, F., D’Esposito, M., 2012. Focal Brain Lesions to Critical Locations Cause Widespread Disruption of the Modular Organization of the Brain. J. Cogn. Neurosci. 24, 1275–1285. https://doi.org/10.1162/jocn_a_00222

Greicius, M.D., Srivastava, G., Reiss, A.L., Menon, V., 2004. Default-mode network activity distinguishes Alzheimer’s disease from healthy aging: evidence from functional MRI. Proc. Natl. Acad. Sci. U. S. A. 101, 4637–42. https://doi.org/10.1073/pnas.0308627101

Greve, D.N., Fischl, B., 2009. Accurate and robust brain image alignment using boundary-based registration. Neuroimage 48, 63–72. https://doi.org/10.1016/j.neuroimage.2009.06.060

Heise, V., Filippini, N., Ebmeier, K.P., Mackay, C.E., 2010. The APOE varepsilon4 allele modulates brain white matter integrity in healthy adults. Mol. Psychiatry 1–9. https://doi.org/10.1038/mp.2010.90

Hellyer, P.J., Scott, G., Shanahan, M., Sharp, D.J., Leech, R., 2015. Cognitive Flexibility through Metastable Neural Dynamics Is Disrupted by Damage to the Structural Connectome. J. Neurosci. 35, 9050–9063. https://doi.org/10.1523/JNEUROSCI.4648-14.2015

Hellyer, P.J., Shanahan, M., Scott, G., Wise, R.J.S., Sharp, D.J., Leech, R., 2014. The control of global brain dynamics: opposing actions of frontoparietal control and default mode networks on attention. J. Neurosci. 34, 451–61. https://doi.org/10.1523/JNEUROSCI.1853-13.2014

Hesse, J., Gross, T., 2014. Self-organized criticality as a fundamental property of neural systems. Front. Syst. Neurosci. 8. https://doi.org/10.3389/fnsys.2014.00166

Honey, C.J., Thivierge, J.-P., Sporns, O., 2010. Can structure predict function in the human brain? Neuroimage 52, 766–76. https://doi.org/10.1016/j.neuroimage.2010.01.071

Hughes, C.P., Berg, L., Danziger, W.L., Coben, L.A., Martin, R.L., 1982. A new clinical scale for the staging of dementia. Br. J. Psychiatry 140, 566–572. https://doi.org/10.1192/bjp.140.6.566

Jack, C.R., Knopman, D.S., Jagust, W.J., Petersen, R.C., Weiner, M.W., Aisen, P.S., Shaw, L.M., Vemuri, P., Wiste, H.J., Weigand, S.D., Lesnick, T.G., Pankratz, V.S., Donohue, M.C., Trojanowski, J.Q., 2013. Tracking pathophysiological processes in Alzheimer's disease: An updated hypothetical model of dynamic biomarkers. Lancet Neurol. https://doi.org/10.1016/S1474-4422(12)70291-0

Jaunmuktane, Z., Mead, S., Ellis, M., Wadsworth, J.D.F., Nicoll, A.J., Kenny, J., Launchbury, F., Linehan, J., Richard-Loendt, A., Walker, A.S., Rudge, P., Collinge, J., Brandner, S., 2015. Evidence for human transmission of amyloid-β pathology and cerebral amyloid angiopathy. Nature 525, 247–250. https://doi.org/10.1038/nature15369

Jenkinson, M., Bannister, P., Brady, M., Smith, S., 2002. Improved optimization for the robust and accurate linear registration and motion correction of brain images. Neuroimage 17, 825–841. https://doi.org/10.1016/S1053-8119(02)91132-8

Jenkinson, M., Smith, S., 2001. A global optimization method for robust affine registration of brain images. Med Image Anal 5, 143–156.

Jones, D.T., Vemuri, P., Murphy, M.C., Gunter, J.L., Senjem, M.L., Machulda, M.M., Przybelski, S. a., Gregg, B.E., Kantarci, K., Knopman, D.S., Boeve, B.F., Petersen, R.C., Jack, C.R., 2012. Non-stationarity in the “resting brain’s” modular architecture. PLoS One 7, e39731. https://doi.org/10.1371/journal.pone.0039731

Kelso, J.A.S., 2012. Multistability and metastability: understanding dynamic coordination in the brain. Philos. Trans. R. Soc. Lond. B. Biol. Sci. 367, 906–18. https://doi.org/10.1098/rstb.2011.0351

Kelso, J.A.S., 2008. The Complementary Nature. MIT Press.

Kelso, J.A.S., 1995. Dynamic Patterns: The Self-Organization of Brain and Behavior. MIT Press.

Kitzbichler, M.G., Henson, R.N.A., Smith, M.L., Nathan, P.J., Bullmore, E.T., 2011. Cognitive Effort Drives Workspace Configuration of Human Brain Functional Networks. J. Neurosci. 31, 8259–8270. https://doi.org/10.1523/JNEUROSCI.0440-11.2011

Kringelbach, M.L., McIntosh, A.R., Ritter, P., Jirsa, V.K., Deco, G., 2015. The Rediscovery of Slowness: Exploring the Timing of Cognition. Trends Cogn. Sci. 19, 616–628. https://doi.org/10.1016/j.tics.2015.07.011

Kundu, P., Hens, C., Barzel, B., Pal, P., 2017. Perfect synchronization in networks of phase-frustrated oscillators. EPL 120. https://doi.org/10.1209/0295-5075/120/40002

Kuramoto, Y., 1984. Chemical Oscillations, Waves, and Turbulence, Springer Series in Synergetics. Springer Berlin Heidelberg, Berlin, Heidelberg. https://doi.org/10.1007/978-3-642-69689-3

Liu, Y., Yu, C., Zhang, X., Liu, J., Duan, Y., Alexander-Bloch, A.F., Liu, B., Jiang, T., Bullmore, E., 2014. Impaired long distance functional connectivity and weighted network architecture in alzheimer’s disease. Cereb. Cortex 24, 1422–1435. https://doi.org/10.1093/cercor/bhs410

Messé, A., Rudrauf, D., Benali, H., Marrelec, G., 2014. Relating Structure and Function in the Human Brain: Relative Contributions of Anatomy, Stationary Dynamics, and Non-stationarities. PLoS Comput. Biol. 10. https://doi.org/10.1371/journal.pcbi.1003530

Moretti, P., Muñoz, M.A., 2013. Griffiths phases and the stretching of criticality in brain networks. Nat. Commun. 4. https://doi.org/10.1038/ncomms3521

Mueller, S.G., Weiner, M.W., Thal, L.J., Petersen, R.C., Jack, C., Jagust, W., Trojanowski, J.Q., Toga, A.W., Beckett, L., 2005. The Alzheimer’s Disease Neuroimaging Initiative. Neuroimaging Clin. N. Am. 15, 869–877. https://doi.org/10.1016/j.nic.2005.09.008

O’Dwyer, L., Lamberton, F., Bokde, A.L.W., Ewers, M., Faluyi, Y.O., Tanner, C., Mazoyer, B., O’Neill, D., Bartley, M., Collins, D.R., Coughlan, T., Prvulovic, D., Hampel, H., 2011a. Multiple indices of diffusion identifies white matter damage in mild cognitive

impairment and Alzheimer's disease. PLoS One 6, e21745. https://doi.org/10.1371/journal.pone.0021745

O'Dwyer, L., Lamberton, F., Bokde, A.L.W., Ewers, M., Faluyi, Y.O., Tanner, C., Mazoyer, B., O'Neill, D., Bartley, M., Collins, D.R., Coughlan, T., Prvulovic, D., Hampel, H., 2011b. Using diffusion tensor imaging and mixed-effects models to investigate primary and secondary white matter degeneration in Alzheimer's disease and mild cognitive impairment. J. Alzheimers. Dis. 26, 667–82. https://doi.org/10.3233/JAD-2011-110137

Palop, J., Mucke, L., 2010. Amyloid-beta Induced Neuronal Disease : From Synapses toward Neural Networks. Nat. Neurosci. 13, 812–818. https://doi.org/10.1038/nn.2583.Amyloid-

Pedersen, M., Omidvarnia, A., 2016. Further Insight into the Brain's Rich-Club Architecture. J. Neurosci. 36, 5675–5676. https://doi.org/10.1523/JNEUROSCI.0754-16.2016

Piccoli, T., Valente, G., Linden, D.E.J., Re, M., Esposito, F., Sack, A.T., Salle, F. Di, 2015. The Default Mode Network and the Working Memory Network Are Not Anti-Correlated during All Phases of a Working Memory Task. PLoS One 10, e0123354. https://doi.org/10.1371/journal.pone.0123354

Ponce-Alvarez, A., Deco, G., Hagmann, P., Romani, G.L., Mantini, D., Corbetta, M., 2015. Resting-State Temporal Synchronization Networks Emerge from Connectivity Topology and Heterogeneity. PLoS Comput. Biol. 11. https://doi.org/10.1371/journal.pcbi.1004100

Power, J.D., Schlaggar, B.L., Lessov-Schlaggar, C.N., Petersen, S.E., 2013. Evidence for hubs in human functional brain networks. Neuron 79, 798–813. https://doi.org/10.1016/j.neuron.2013.07.035

Raj, A., Kuceyeski, A., Weiner, M., 2012. A network diffusion model of disease progression in dementia. Neuron 73, 1204–15. https://doi.org/10.1016/j.neuron.2011.12.040

Reuter, M., Rosas, H.D., Fischl, B., 2010. Highly accurate inverse consistent registration: A robust approach. Neuroimage 53, 1181–1196. https://doi.org/10.1016/j.neuroimage.2010.07.020

Rubinov, M., Sporns, O., 2010. Complex network measures of brain connectivity: Uses and interpretations. Neuroimage 52, 1059–1069. https://doi.org/10.1016/j.neuroimage.2009.10.003

Sachdev, P.S., Zhuang, L., Braidy, N., Wen, W., 2013. Is Alzheimer's a disease of the white matter? Curr. Opin. Psychiatry 26, 244–251. https://doi.org/10.1097/YCO.0b013e32835ed6e8

Schacter, D.L., Addis, D.R., Buckner, R.L., 2008. Episodic simulation of future events: Concepts, data, and applications. Ann. N. Y. Acad. Sci. https://doi.org/10.1196/annals.1440.001

Schacter, D.L., Addis, D.R., Buckner, R.L., 2007. Remembering the past to imagine the future: The prospective brain. Nat. Rev. Neurosci. https://doi.org/10.1038/nrn2213

Schilbach, L., Eickhoff, S.B., Rotarska-Jagiela, A., Fink, G.R., Vogeley, K., 2008. Minds at rest? Social cognition as the default mode of cognizing and its putative relationship to the "default system" of the brain. Conscious. Cogn. 17, 457–467. https://doi.org/10.1016/j.concog.2008.03.013

Schirner, M., Rothmeier, S., Jirsa, V.K., McIntosh, A.R., Ritter, P., 2015. An automated pipeline for constructing personalised virtual brains from multimodal neuroimaging data. Neuroimage 117, 343–357. https://doi.org/10.1016/j.neuroimage.2015.03.055

Seeley, W.W., Crawford, R.K., Zhou, J., Miller, B.L., Greicius, M.D., 2009. Neurodegenerative Diseases Target Large-Scale Human Brain Networks. Neuron 62, 42–52. https://doi.org/10.1016/j.neuron.2009.03.024

Ségonne, F., Pacheco, J., Fischl, B., 2007. Geometrically accurate topology-correction of cortical surfaces using nonseparating loops. IEEE Trans. Med. Imaging 26, 518–529. https://doi.org/10.1109/TMI.2006.887364

Senden, M., Deco, G., De Reus, M.A., Goebel, R., Van Den Heuvel, M.P., 2014. Rich club organization supports a diverse set of functional network configurations. Neuroimage 96, 174–182. https://doi.org/10.1016/j.neuroimage.2014.03.066

Shanahan, M., 2010. Metastable chimera states in community-structured oscillator networks. Chaos 20, 13108. https://doi.org/10.1063/1.3305451

Shew, W.L., Plenz, D., 2013. The Functional Benefits of Criticality in the Cortex. Neurosci. 19, 88–100. https://doi.org/10.1177/1073858412445487

Sled, J.G., Zijdenbos, a P., Evans, a C., 1998. A nonparametric method for automatic correction of intensity nonuniformity in MRI data. IEEE Trans. Med. Imaging 17, 87–97. https://doi.org/10.1109/42.668698

Smith, K.D.B., Kallhoff, V., Zheng, H., Pautler, R.G., 2007. In vivo axonal transport rates decrease in a mouse model of Alzheimer's disease. Neuroimage 35, 1401–1408. https://doi.org/10.1016/j.neuroimage.2007.01.046

Smith, S.M., Fox, P.T., Miller, K.L., Glahn, D.C., Fox, P.M., Mackay, C.E., Filippini, N., Watkins, K.E., Toro, R., Laird, A.R., Beckmann, C.F., 2009. Correspondence of the brain' s functional architecture during activation and rest. Proc. Natl. Acad. Sci. U. S. A. 106, 13040–13045. https://doi.org/10.1073/pnas.0905267106

Sporns, O., 2013. Structure and function of complex brain networks. Dialogues Clin. Neurosci. 15, 247–262. https://doi.org/10.1137/S003614450342480

Spreng, R.N., Mar, R.A., Kim, A.S.N., 2009. The Common Neural Basis of Autobiographical Memory, Prospection, Navigation, Theory of Mind, and the Default Mode: A Quantitative Meta-analysis. J. Cogn. Neurosci. 21, 489–510. https://doi.org/10.1162/jocn.2008.21029

Spreng, R.N., Stevens, W.D., Chamberlain, J.P., Gilmore, A.W., Schacter, D.L., 2010. Default network activity, coupled with the frontoparietal control network, supports goal-directed cognition. Neuroimage 53, 303–317. https://doi.org/10.1016/j.neuroimage.2010.06.016

Strogatz, S.H., 2000. From Kuramoto to Crawford: exploring the onset of synchronization in populations of coupled oscillators. Phys. D Nonlinear Phenom. 143, 1–20. https://doi.org/10.1016/S0167-2789(00)00094-4

Tagliazucchi, E., Balenzuela, P., Fraiman, D., Chialvo, D.R., 2012. Criticality in large-scale brain fmri dynamics unveiled by a novel point process analysis. Front. Physiol. 3 FEB. https://doi.org/10.3389/fphys.2012.00015

Teipel, S.J., Grothe, M.J., Filippi, M., Fellgiebel, A., Dyrba, M., Frisoni, G.B., Meindl, T., Bokde, A.L.W., Hampel, H., Kl??ppel, S., Hauenstein, K., 2014. Fractional anisotropy changes in Alzheimer's disease depend on the underlying fiber tract architecture: A multiparametric DTI study using joint independent component analysis. J. Alzheimer's Dis. 41, 69–83. https://doi.org/10.3233/JAD-131829

Therriault, J., Ng, K.P., Pascoal, T.A., Mathotaarachchi, S., Kang, M.S., Struyfs, H., Shin, M., Benedet, A.L., Walpola, I.C., Nair, V., Gauthier, S., Rosa-Neto, P., Alzheimer's Disease Neuroimaging Initiative, F. the A.D.N., 2018. Anosognosia predicts default mode network hypometabolism and clinical progression to dementia. Neurology 90, e932–e939. https://doi.org/10.1212/WNL.0000000000005120

Tijms, B.M., Wink, A.M., de Haan, W., van der Flier, W.M., Stam, C.J., Scheltens, P., Barkhof, F., 2013. Alzheimer's disease: connecting findings from graph theoretical studies of brain networks. Neurobiol. Aging 34, 2023–2036. https://doi.org/10.1016/j.neurobiolaging.2013.02.020

Tognoli, E., Kelso, J.A.S., 2014a. The Metastable Brain. Neuron 81, 35–48. https://doi.org/10.1016/j.neuron.2013.12.022

Tognoli, E., Kelso, J.A.S., 2014b. Enlarging the scope: grasping brain complexity. Front. Syst. Neurosci. 8, 122. https://doi.org/10.3389/fnsys.2014.00122

Tognoli, E., Kelso, J.A.S., 2009. Brain coordination dynamics: True and false faces of phase synchrony and metastability. Prog. Neurobiol. 87, 31–40. https://doi.org/10.1016/j.pneurobio.2008.09.014

Tournier, J.-D., Calamante, F., Connelly, A., 2012. MRtrix: Diffusion tractography in crossing fiber regions. Int. J. Imaging Syst. Technol. 22, 53–66. https://doi.org/10.1002/ima.22005

Tournier, J.-D., Calamante, F., Gadian, D.G., Connelly, A., 2004. Direct estimation of the fiber orientation density function from diffusion-weighted MRI data using spherical deconvolution. Neuroimage 23, 1176–85. https://doi.org/10.1016/j.neuroimage.2004.07.037

Uhlhaas, P.J., 2015. Neural dynamics in mental disorders. World Psychiatry 14, 116–8. https://doi.org/10.1002/wps.20203

Uhlhaas, P.J., Singer, W., 2006. Neural Synchrony in Brain Disorders: Relevance for Cognitive Dysfunctions and Pathophysiology. Neuron. https://doi.org/10.1016/j.neuron.2006.09.020

van den Heuvel, M.P., Kahn, R.S., Goni, J., Sporns, O., 2012. High-cost, high-capacity backbone for global brain communication. Proc. Natl. Acad. Sci. 109, 11372–11377. https://doi.org/10.1073/pnas.1203593109

van den Heuvel, M.P., Sporns, O., 2011. Rich-club organization of the human connectome. J. Neurosci. 31, 15775–86. https://doi.org/10.1523/JNEUROSCI.3539-11.2011

Váša, F., Shanahan, M., Hellyer, P.J., Scott, G., Cabral, J., Leech, R., 2015. Effects of lesions on synchrony and metastability in cortical networks. Neuroimage 118, 456–67. https://doi.org/10.1016/j.neuroimage.2015.05.042

Vincent, J.L., Kahn, I., Snyder, A.Z., Raichle, M.E., Buckner, R.L., 2008. Evidence for a Frontoparietal Control System Revealed by Intrinsic Functional Connectivity. J. Neurophysiol. 100, 3328–3342. https://doi.org/10.1152/jn.90355.2008

Warren, D.E., Power, J.D., Bruss, J., Denburg, N.L., Waldron, E.J., Sun, H., Petersen, S.E., Tranel, D., 2014. Network measures predict neuropsychological outcome after brain injury. Proc. Natl. Acad. Sci. 111, 14247–14252. https://doi.org/10.1073/pnas.1322173111

Wechsler, D., 1987. Manual for Wechsler Memory Scale - Revised, The Psychological Corporation. https://doi.org/PCA-Converted #56

Wildie, M., Shanahan, M., 2012. Metastability and chimera states in modular delay and pulse-coupled oscillator networks. Chaos 22, 43131. https://doi.org/10.1063/1.4766592

Wirths, O., Weis, J., Kayed, R., Saido, T.C., Bayer, T.A., 2007. Age-dependent axonal degeneration in an Alzheimer mouse model. Neurobiol. Aging 28, 1689–1699. https://doi.org/10.1016/j.neurobiolaging.2006.07.021

Wirths, O., Weis, J., Szczygielski, J., Multhaup, G., Bayer, T.A., 2006. Axonopathy in an APP/PS1 transgenic mouse model of Alzheimer's disease. Acta Neuropathol. 111, 312–319. https://doi.org/10.1007/s00401-006-0041-4

Yang, H., Shew, W.L., Roy, R., Plenz, D., 2012. Maximal Variability of Phase Synchrony in Cortical Networks with Neuronal Avalanches. J. Neurosci. 32, 1061–1072. https://doi.org/10.1523/JNEUROSCI.2771-11.2012

Zalesky, A., Fornito, A., Bullmore, E.T., 2010. Network-based statistic: Identifying differences in brain networks. Neuroimage 53, 1197–1207. https://doi.org/10.1016/j.neuroimage.2010.06.041

Zalesky, A., Fornito, A., Cocchi, L., Gollo, L.L., Breakspear, M., 2014. Time-resolved resting-state brain networks. Proc. Natl. Acad. Sci. U. S. A. 111, 10341–6. https://doi.org/10.1073/pnas.1400181111

Zhao, Q., Lu, H., Metmer, H., Li, W.X.Y., Lu, J., 2018. Evaluating functional connectivity of executive control network and frontoparietal network in Alzheimer's disease. Brain Res. 1678, 262–272. https://doi.org/10.1016/j.brainres.2017.10.025

Zhou, J., Gennatas, E.D., Kramer, J.H., Miller, B.L., Seeley, W.W., 2012. Predicting regional neurodegeneration from the healthy brain functional connectome. Neuron 73, 1216–27. https://doi.org/10.1016/j.neuron.2012.03.004

Zhuang, L., Sachdev, P.S., Trollor, J.N., Kochan, N.A., Reppermund, S., Brodaty, H., Wen, W., 2012. Microstructural white matter changes in cognitively normal individuals at risk of amnestic MCI. Neurology 79, 748–754. https://doi.org/10.1212/WNL.0b013e3182661f4d